

A Deep Signed Directional Distance Function for Object Shape Representation

Ehsan Zobeidi Nikolay Atanasov
 University of California, San Diego
 {ezobeidi, natanasov}@ucsd.edu

Abstract

Neural networks that map 3D coordinates to signed distance function (SDF) or occupancy values have enabled high-fidelity implicit representations of object shape. This paper develops a new shape model that allows synthesizing novel distance views by optimizing a continuous signed directional distance function (SDDF). Similar to deep SDF models, our SDDF formulation can represent whole categories of shapes and complete or interpolate across shapes from partial input data. Unlike an SDF, which measures distance to the nearest surface in any direction, an SDDF measures distance in a given direction. This allows training an SDDF model without 3D shape supervision, using only distance measurements, readily available from depth camera or Lidar sensors. Our model also removes post-processing steps like surface extraction or rendering by directly predicting distance at arbitrary locations and viewing directions. Unlike deep view-synthesis techniques, such as Neural Radiance Fields, which train high-capacity black-box models, our model encodes by construction the property that SDDF values decrease linearly along the viewing direction. This structure constraint not only results in dimensionality reduction but also provides analytical confidence about the accuracy of SDDF predictions, regardless of the distance to the object surface.

1. Introduction

Geometric understanding of object shape is a central problem for enabling task specification, environment interaction, and safe navigation for autonomous systems. Various models of object shape have been proposed to facilitate recognition, classification, rendering, reconstruction, etc. There is no universal 3D shape representation because different models offer different advantages. For example, explicit shape models based on polygonal meshes allow accurate representation of surfaces and texture and lighting properties. Generative mesh modeling [17, 50], however, is very challenging as it requires predicting the mesh topology and the number of vertices. Impressive results have

been achieved recently with implicit shape models, representing surfaces as the zero level set of a deep neural network approximation of signed distance function (SDF) [32] or occupancy field [26]. Many implicit surface techniques, however, require 3D shape supervision and post-processing in the form of surface extraction and distance computation [13]. Deep view synthesis models [27] offer an alternative to directly synthesize texture, lighting, and distance, avoiding surface extraction or differentiable rendering.

This paper enables implicit shape description by learning a model capable of novel distance view synthesis. We represent an object shape as a continuous function $h(\mathbf{p}, \boldsymbol{\eta})$ which measures the (signed) distance to the object surface from a given 3D position \mathbf{p} and unit-norm viewing direction $\boldsymbol{\eta}$. We refer to such a function as a signed directional distance function (SDDF). Compared to an SDF, approximating an SDDF with a neural network appears more challenging due to the additional two-degree-of-freedom input $\boldsymbol{\eta}$. With a naive model, there is no guarantee that the parameter optimization converges to the correct object geometry as the input degrees of freedom increase. This challenge is evident even in SDF models, where learned distances are only accurate close to the surface and surface extraction is necessary to predict distances far away from the object boundary. Inspired by Gropp et al. [11] who observe that a valid SDF must satisfy an Eikonal differential equation, we obtain a differential equation capturing the fact that SDDF values decrease linearly along the viewing direction. We design a neural network architecture for learning SDDFs that ensures *by construction* that the SDDF gradient property is satisfied. This not only results in dimensionality reduction but also provides analytical confidence that the accuracy of an SDDF model is independent of the distance of the training or testing points to the object surface. More precisely, training the model to accurately predict SDDF values everywhere does not need dense sampling of the domain. The particular distance of the training samples to the object surface is not important, leading to a reduction in the number of necessary training samples. Because an SDDF outputs distance to the object surfaces directly, our model can be trained without 3D supervision, using distance measure-

ments from depth camera or Lidar sensors.

Nonetheless, training an SDDF model requires distance data from different orientations η (unlike an SDF model). To avoid the need for a large training set with distance data from many views, we develop a data augmentation technique for distance data synthesis from new positions and orientations. Given a point cloud observation of the object surface, we decide which points would be visible from a desired view using spherical projection and convex hull approximation. Our data augmentation technique ensures that we can train a multi-view consistency SDDF model even from a small training set with a few distance views.

Inspired by DeepSDF [32], we extend the SDDF model to enable category-level shape description. Instances from the same object category possess similar geometric structure. Training a different shape model for each instance is inefficient and impractical. We introduce a category-level SDDF auto-decoder and an instance-level latent shape code to represent the geometry of a class of shapes. We show that a trained SDDF model is capable of interpolating between the latent shape codes of different instances, while generating valid shapes and distance views at intermediate points. Optimizing the latent code at test time also allows shape completion of previously unseen instances from a small set of distance samples.

In summary, we make the following contributions.

- We propose a new signed directional distance function to model continuous distance view synthesis.
- We derive structural properties satisfied by SDDFs and encode them in the design of a neural network architecture for SDDF learning.
- We propose a data augmentation technique to ensure that a multi-view consistent SDDF model can be trained from a small dataset.
- We demonstrate that an SDDF model, augmented with a latent shape code, is capable of representing a category of shapes, enabling shape completion and shape interpolation without 3D supervision.

Our model is demonstrated in qualitative and quantitative experiments using the ShapeNet dataset [4].

2. Related Works

This section reviews 3D shape modeling techniques.

Mesh models: Several memory efficient explicit mesh representations of shape have been proposed [3, 9, 19, 45, 46, 61, 65]. Object surfaces may be viewed as a collection of connected charts, parameterized by a neural network [23, 42, 52]. AtlasNet [12] parametrizes each chart with a multi-layer perceptron that maps a flat square to the real chart. Deep geometric prior (DGP) [52] improves the results using Wasserstein distance and enforcing a consistency condition to fit the charts.

Geometric primitive models: PointNet [35] proposes a new architecture for point cloud feature extraction that respects the permutation invariance of point clouds. Shape completion from partial point cloud data is investigated by [12, 22, 48, 54, 58, 62] using an encoder-decoder structure to estimate the point cloud of unseen shapes. Generative adversarial networks and adversarial auto-encoders have been employed recently for point cloud shape synthesis [1, 20, 41, 53, 56, 60]. Point cloud models, however, do not provide continuous shape representations. In cases where a coarse model is sufficient, 3D volumetric primitives can be used [50], including cuboids [57] or quadrics [30, 33].

Grid-based models: Discretizing 3D space into a regular or adaptive grid to store occupancy [7, 47] is another popular representation. OctNet [37, 38] defines convolution directly over octrees, exploiting the sparsity and hierarchical partitioning of 3D space. Octrees may be used to store a truncated signed distance function whose zero level set corresponds with the object surface [6, 8, 26, 63]. Choosing voxels close to the surface and using a kernel to predict continuous truncated SDF values improves the accuracy [67].

Deep signed distance models: DeepSDF [32] develops an auto-decoder model for approximating continuous SDF values and enables learning category-level shape through a latent shape code. This work demonstrated that various object topologies can be captured as differentiable implicit functions, inspiring interest in learned SDF representations [10, 16, 21, 43, 44, 55]. IGR [11] improves the method by incorporating a unit-norm gradient constraint on the SDF values in the training loss function. IDR [59] extends the SDF model to simultaneously learn geometry, camera parameters, and a neural renderer that approximates the light reflected towards the camera. MVSDF [64] optimizes an SDF and a light field appearance model jointly, supervised by image features and depth from a multi-view stereo network. A-SDF [28] represents articulated shapes with a disentangled latent space, including separate codes for encoding shape and articulation.

View synthesis models: Niemeyer et al. [31] enable differentiable rendering of implicit shape and texture representations by deriving the gradients of the predicted depth map with respect to the network parameters. NeRF [24, 27, 40] learns to predict the volume density and radiance of a scene at arbitrary positions and viewing directions using RGB images as input. NeRF is trained as a high-capacity black-box model and does not capture the property that distances decrease linearly along the viewing direction. IBRNet [51] uses a multilayer perceptron and a ray transformer to estimate the radiance and volume density at continuous position and view locations from a sparse set of nearby views. GRF [49] is a neural network model for implicit radiance field representation and rendering of 3D objects, trained by aggregating pixel features from multiple 2D views. MVS-

NeRF [5] extends deep multi-view stereo methods to reason about both scene geometry and appearance and output a neural radiance field. This radiance field model can be fine-tuned on novel test scenes significantly faster than a NeRF model. DietNeRF [15] introduces an auxiliary semantic consistency loss that encourages realistic renderings at novel poses. This allows supervising DietNeRF from arbitrary poses leading to high-quality scene reconstruction with as few as 8 training views.

3. Problem Statement

We focus on learning shape representations for object instances from a known category, e.g., car, airplane, chair, etc. In contrast with most existing work for shape modeling which relies on 3D CAD models for training, we only consider distance measurement data, e.g., obtained from a depth camera or a Lidar scanner. We model a distance sensor measurement as a collection of rays (e.g, corresponding to depth camera pixels or Lidar beams) along which the distance from the sensor position (e.g., depth camera optical center or Lidar sensor frame origin) to the nearest surface is measured. Let $\boldsymbol{\eta}_i \in S^{n-1} := \{\boldsymbol{\eta} \in \mathbb{R}^n \mid \|\boldsymbol{\eta}\|_2 = 1\}$ denote a unit-vector in the direction of ray i with associated distance measurement $d_i \in (\underline{d}, \bar{d}) \cup \{\infty\}$ obtained from sensor position $\mathbf{p}_i \in \mathbb{R}^n$. In practice, the dimension n is 2 or 3 and the measurements are limited by a minimum distance $\underline{d} > 0$ and a maximum distance $\bar{d} < \infty$. The measurements of rays that do not hit a surface are set to ∞ . We consider the following shape representation problem.

Problem 1. Let $\mathcal{D}_l := \{(\mathbf{p}_{i,l}, \boldsymbol{\eta}_{i,l}, d_{i,l})\}_i$ be sets of distance measurements obtained from different instances l from the same object category. Learn a latent shape encoding $\mathbf{z}_l \in \mathbb{R}^m$ for each instance l and a function $h(\mathbf{p}, \boldsymbol{\eta}, \mathbf{z})$ that can predict the distance from any point \mathbf{p} along any direction $\boldsymbol{\eta}$ to the surface of any instance with shape \mathbf{z} .

4. Method

This section proposes a new signed directional distance representation of object shape (Sec. 4.1), studies its properties (Sec. 4.2, Sec. 4.3), and proposes a neural network architecture, cost function, and data augmentation technique for learning such shape representations (Sec. 4.4, Sec. 4.5).

4.1. Signed Directional Distance Function

We propose a signed directional distance function to model the data generated by distance sensors.

Definition 1. The *signed directional distance function* (SDDF) $h : \mathbb{R}^n \times S^{n-1} \mapsto \mathbb{R}$ of a set $\mathcal{O} \subset \mathbb{R}^n$ measures the signed distance from a point $\mathbf{p} \in \mathbb{R}^n$ to the set boundary

$\partial\mathcal{O}$ in direction $\boldsymbol{\eta} \in S^{n-1}$:

$$\begin{aligned} h(\mathbf{p}, \boldsymbol{\eta}) &:= d_{\boldsymbol{\eta}}(\mathbf{p}, \partial\mathcal{O}), \\ d_{\boldsymbol{\eta}}(\mathbf{p}, \partial\mathcal{O}) &:= \min \{d \in \mathbb{R} \mid \mathbf{p} + d\boldsymbol{\eta} \in \partial\mathcal{O}\}. \end{aligned} \quad (1)$$

Unlike an SDF, which measures the distance to the nearest surface in *any* direction, an SDDF measures the distance to the nearest surface in a *specific* direction. Also, unlike an SDF, which is negative inside the surface that it models, and SDDF is negative behind the observer’s point of view. A key property is that, if the SDDF of a set is known, we can generate arbitrary distance views to the set boundary. In other words, we can image what a distance sensor would see from any point \mathbf{p} in any viewing direction $\boldsymbol{\eta}$.

We focus on learning SDDF representations using distance measurements as in Problem 1. We propose a neural network architecture that, by design, captures the structure of an SDDF. Note that for a fixed viewing direction $\boldsymbol{\eta}$, an SDDF satisfies $h(\mathbf{p}_1, \boldsymbol{\eta}) - h(\mathbf{p}_2, \boldsymbol{\eta}) = (\mathbf{p}_2 - \mathbf{p}_1)^\top \boldsymbol{\eta}$ for points $\mathbf{p}_1, \mathbf{p}_2$ along the ray $\boldsymbol{\eta}$ that are close to each other, in the sense that they see the same nearest point on the set surface. This property is formalized below.

Lemma 1. *The gradient of an SDDF $h(\mathbf{p}, \boldsymbol{\eta})$ with respect to \mathbf{p} projected to the viewing direction $\boldsymbol{\eta}$ satisfies:*

$$\nabla_{\mathbf{p}} h(\mathbf{p}, \boldsymbol{\eta})^\top \boldsymbol{\eta} = -1. \quad (2)$$

4.2. SDDF Structure

In this section, we propose a neural network parameterization of a function $h(\mathbf{p}, \boldsymbol{\eta})$ that satisfies the condition in (2) by construction. First, we simplify the requirement that the gradient in (2) is non-zero by defining a function $g(\mathbf{p}, \boldsymbol{\eta}) := h(\mathbf{p}, \boldsymbol{\eta}) + \mathbf{p}^\top \boldsymbol{\eta}$. Note that (2) is equivalent to:

$$\nabla_{\mathbf{p}} g(\mathbf{p}, \boldsymbol{\eta})^\top \boldsymbol{\eta} = 0. \quad (3)$$

Next, we show that (3) implies that one degree of freedom should be removed from the domain of $g(\mathbf{p}, \boldsymbol{\eta})$. Our idea is to rotate \mathbf{p} and $\boldsymbol{\eta}$ so that viewing direction $\boldsymbol{\eta}$ becomes the unit vector $\mathbf{e}_n = [0, \dots, 0, 1]^\top$ along the last coordinate axis in the sensor frame. This rotation will show that the third element of the gradient of $g(\mathbf{p}, \boldsymbol{\eta})$ should be zero, implying that $g(\mathbf{p}, \boldsymbol{\eta})$ is constant along the third dimension in the rotated reference frame. The rotation matrix $\mathbf{R} \in SO(n)$ that maps a unit vector $\mathbf{x} \in S^{n-1}$ to another unit vector $\mathbf{y} \in S^{n-1}$ with $\mathbf{y} \neq -\mathbf{x}$ along the sphere geodesic (shortest path) is [2]:

$$\mathbf{R} = \mathbf{I} + \mathbf{y}\mathbf{x}^\top - \mathbf{x}\mathbf{y}^\top + \frac{1}{1 + \mathbf{x}^\top \mathbf{y}} (\mathbf{y}\mathbf{x}^\top - \mathbf{x}\mathbf{y}^\top)^2. \quad (4)$$

Using (4), we can obtain an explicit expression for the rotation matrix $\mathbf{R}_{\boldsymbol{\eta}}$ that maps $\boldsymbol{\eta}$ to \mathbf{e}_n .

Lemma 2. A vector $\boldsymbol{\eta} = [a, b]^\top \in S^1$ can be mapped to $\mathbf{e}_2 \in S^1$ via the rotation matrix $\mathbf{R}_\boldsymbol{\eta} := \begin{bmatrix} b & -a \\ a & b \end{bmatrix} \in SO(2)$.

Lemma 3. A vector $\boldsymbol{\eta} = [a, b, c]^\top \in S^2$ can be mapped to $\mathbf{e}_3 \in S^2$ via the rotation matrix $\mathbf{R}_\boldsymbol{\eta} \in SO(3)$ below:

$$\mathbf{R}_\boldsymbol{\eta} := \begin{cases} \begin{bmatrix} 1 & 0 & 0 \\ 0 & 1 & 0 \\ 0 & 0 & -1 \end{bmatrix} & \text{if } \boldsymbol{\eta} = -\mathbf{e}_3, \\ \begin{bmatrix} 1 - \frac{a^2}{1+c} & -\frac{ab}{1+c} & -a \\ -\frac{ab}{1+c} & 1 - \frac{b^2}{1+c} & -b \\ a & b & c \end{bmatrix} & \text{otherwise.} \end{cases} \quad (5)$$

Using $\mathbf{R}_\boldsymbol{\eta}$, we can express the condition in (3) in a rotated coordinate frame where $\mathbf{q} = \mathbf{R}_\boldsymbol{\eta}\mathbf{p}$. By the chain rule:

$$0 = \frac{dg}{d\mathbf{p}}\boldsymbol{\eta} = \frac{dg}{dq} \frac{dq}{d\mathbf{p}}\boldsymbol{\eta} = \frac{dg}{dq}\mathbf{R}_\boldsymbol{\eta}\boldsymbol{\eta} = \frac{dg}{dq}\mathbf{e}_n = \frac{dg}{dq_n}. \quad (6)$$

The set of functions that satisfy (6) do not depend on the last element of \mathbf{q} or, in other words, can be expressed as $g(\mathbf{p}, \boldsymbol{\eta}) = f(\mathbf{P}\mathbf{R}_\boldsymbol{\eta}\mathbf{p}, \boldsymbol{\eta})$ for a projection matrix $\mathbf{P} := [\mathbf{I} \ \mathbf{0}] \in \mathbb{R}^{(n-1) \times n}$ and some function f . This elucidates the structure of signed directional distance functions.

Proposition 1. Learning a function $f : \mathbb{R}^{n-1} \times S^{n-1} \mapsto \mathbb{R}$ guarantees that $h(\mathbf{p}, \boldsymbol{\eta}) := f(\mathbf{P}\mathbf{R}_\boldsymbol{\eta}\mathbf{p}, \boldsymbol{\eta}) - \mathbf{p}^\top \boldsymbol{\eta}$ is an SDDF (Def. 1) and satisfies (2) in Lemma 1.

4.3. Infinite SDDF Values

Proposition 1 allows learning SDDF representations of object shape from distance measurements without the need to enforce structure constraints explicitly. An additional challenge, however, is that real distance sensors have a limited field of view and, hence, the SDDF values $h(\mathbf{p}, \boldsymbol{\eta})$ at some sensor positions \mathbf{p} and viewing directions $\boldsymbol{\eta}$ (e.g., not directly looking toward the object) will be infinite. We cannot expect a regression model to predict infinite values directly. We introduce an invertible function ϕ to condition the distance data by squashing the values to a finite range.

Lemma 4. Let $\phi : \mathbb{R} \mapsto \mathbb{R}$ be a function with non-zero derivative, $\phi'(x) \neq 0$, for all $x \in \mathbb{R}$. Then, for any function $g : \mathbb{R}^n \times S^{n-1} \mapsto \mathbb{R}$ and vector $\boldsymbol{\eta} \in S^{n-1}$, we have:

$$\nabla_{\mathbf{p}} g(\mathbf{p}, \boldsymbol{\eta})^\top \boldsymbol{\eta} = 0 \quad \text{iff} \quad \nabla_{\mathbf{p}} \phi(g(\mathbf{p}, \boldsymbol{\eta}))^\top \boldsymbol{\eta} = 0. \quad (7)$$

Proof. The claim is concluded by the chain rule, $0 = \nabla_{\mathbf{p}} \phi(g(\mathbf{p}, \boldsymbol{\eta}))^\top \boldsymbol{\eta} = \phi'(g(\mathbf{p}, \boldsymbol{\eta})) \nabla_{\mathbf{p}} g(\mathbf{p}, \boldsymbol{\eta})^\top \boldsymbol{\eta}$ and since $\phi'(g(\mathbf{p}, \boldsymbol{\eta}))$ is never zero. \square

Since ϕ' is never zero, ϕ is either strictly increasing or strictly decreasing by the mean value theorem. In both cases, it has an inverse ϕ^{-1} . Useful examples of such

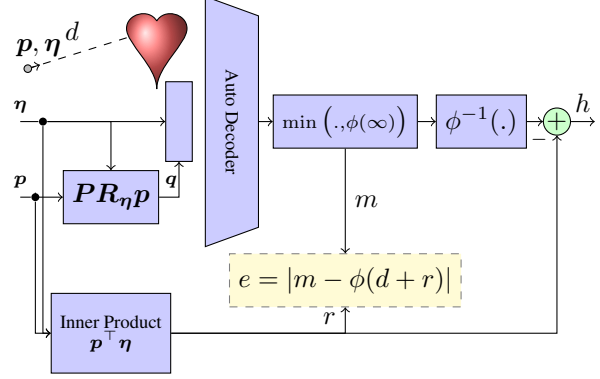


Figure 1. Neural network model for SDDF approximation. Given a position \mathbf{p} , viewing direction $\boldsymbol{\eta}$ and measured distance d , the model rotates \mathbf{p} to new coordinates $\mathbf{R}_\boldsymbol{\eta}\mathbf{p}$, whose last component does not effect the SDDF value. The projected input \mathbf{q} is processed by an autoencoder to predict a squashed distance value m , which may be converted to an SDDF value h or compared to a modified distance $d + \mathbf{p}^\top \boldsymbol{\eta}$ in the error function.

functions, which can be used to squash the distance values to a finite range, include logistic sigmoid $\sigma(x) := (1 + \exp(-x))^{-1}$, hyperbolic tangent $\tanh(x)$, and the Gaussian error function $\text{erf}(x)$. Hereafter we assume ϕ is strictly increasing and define $q(\mathbf{p}, \boldsymbol{\eta}) := \phi(f(\mathbf{P}\mathbf{R}_\boldsymbol{\eta}\mathbf{p}, \boldsymbol{\eta}))$ such that as in Proposition 1:

$$h(\mathbf{p}, \boldsymbol{\eta}) = \phi^{-1}(q(\mathbf{p}, \boldsymbol{\eta})) - \mathbf{p}^\top \boldsymbol{\eta}. \quad (8)$$

This formulation allows training of and inference with a neural network parameterization of $q(\mathbf{p}, \boldsymbol{\eta})$ with possibly infinite distance values. Due to Lemma 4, (8) is still guaranteed to satisfy the SDDF property $\nabla_{\mathbf{p}} h(\mathbf{p}, \boldsymbol{\eta})^\top \boldsymbol{\eta} = -1$.

4.4. SDDF Learning

Fig. 1 shows a neural network model for learning an SDDF representation.

Single-Instance SDDF Training: Given distance measurements \mathcal{D}_l , as in Problem 1, from a single object instance l , we can learn an SDDF representation $h(\mathbf{p}, \boldsymbol{\eta})$ in (8) of the instance shape by optimizing the parameters of a neural network model $q_\theta(\mathbf{p}, \boldsymbol{\eta})$ with structure described in Sec. 5.

We split the training data \mathcal{D}_l into two sets, distinguishing whether the distance measurements are finite or infinite:

$$\begin{aligned} \mathcal{F}_l &:= \{(\mathbf{p}, \boldsymbol{\eta}, d) \in \mathcal{D}_l \mid d < \infty\}, \\ \mathcal{I}_l &:= \{(\mathbf{p}, \boldsymbol{\eta}, d) \in \mathcal{D}_l \mid d = \infty\}, \end{aligned} \quad (9)$$

and define an error function for training the parameters $\boldsymbol{\theta}$:

$$\begin{aligned} e(\boldsymbol{\theta}; \mathcal{F}, \mathcal{I}) &:= \frac{\alpha}{|\mathcal{F}|} \sum_{(\mathbf{p}, \boldsymbol{\eta}, d) \in \mathcal{F}} |\phi(d + \mathbf{p}^\top \boldsymbol{\eta}) - q_\theta(\mathbf{p}, \boldsymbol{\eta})|^p \\ &+ \frac{\beta}{|\mathcal{I}|} \sum_{(\mathbf{p}, \boldsymbol{\eta}, d) \in \mathcal{I}} r (\phi(\infty) - q_\theta(\mathbf{p}, \boldsymbol{\eta}))^p + \gamma \|\boldsymbol{\theta}\|_p^p, \end{aligned} \quad (10)$$

where $\alpha, \beta, \gamma > 0$ are weights, $p \geq 1$, and r is a rectifier, such as ReLU $r(x) = \max\{0, x\}$, GELU $r(x) = x\Phi(x)$, or softplus $r(x) = \log(1 + \exp(x))$. In the experiments, we use $p = 1$ and $r(x) = \max\{0, x\}$. The last term in (10) regularizes the network parameters θ , but in all experiments we set the γ to zero. The first term encourages $q_\theta(\mathbf{p}, \boldsymbol{\eta})$ to predict the squashed distance values accurately. We introduced a rectifier r in the second term in (10) to allow the output of $q_\theta(\mathbf{p}, \boldsymbol{\eta})$ to exceed $\phi(\infty)$, which we observed empirically leads to faster convergence. To address that $q_\theta(\mathbf{p}, \boldsymbol{\eta})$ may exceed $\phi(\infty)$, we modify its conversion to an SDDF as:

$$h(\mathbf{p}, \boldsymbol{\eta}) = \phi^{-1}(\min\{q_\theta(\mathbf{p}, \boldsymbol{\eta}), \phi(\infty)\}) - \mathbf{p}^\top \boldsymbol{\eta}. \quad (11)$$

Multi-Instance SDDF Training: Next, we consider learning an SDDF shape model for multiple instances l from the same category with common parameters θ . Inspired by DeepSDF [32], we introduce a latent code $\mathbf{z}_l \in \mathbb{R}^m$ to model the shape of each instance l and learn it as part of the neural network parameters with structure $q_\theta(\mathbf{p}, \boldsymbol{\eta}, \mathbf{z}_l)$ described in Sec. 5. Given distance measurements \mathcal{F}_l and \mathcal{I}_l , we optimize \mathbf{z}_l independently, for each instance l , and θ jointly, across all instances using the same error as in (10):

$$\begin{aligned} \min_{\theta, \{\mathbf{z}_l\}_l} & \frac{\alpha}{\sum_l |\mathcal{F}_l|} \sum_l \sum_{(\mathbf{p}, \boldsymbol{\eta}, d) \in \mathcal{F}_l} |\phi(d + \mathbf{p}^\top \boldsymbol{\eta}) - q_\theta(\mathbf{p}, \boldsymbol{\eta}, \mathbf{z}_l)|^p \\ & + \frac{1}{\sum_l |\mathcal{I}_l|} \sum_l \sum_{(\mathbf{p}, \boldsymbol{\eta}, d) \in \mathcal{I}_l} \beta r(\phi(\infty) - q_\theta(\mathbf{p}, \boldsymbol{\eta}, \mathbf{z}_l))^p + \sigma \|\mathbf{z}_l\|_p^p + \gamma \|\theta\|_p^p. \end{aligned}$$

Online Shape Optimization: Finally, we consider a shape completion task, where we predict the SDDF shape of a previously unseen instance from partial distance measurements \mathcal{F}, \mathcal{I} . In this case, we assume that the category-level neural network parameters θ are already trained offline and we have an average category-level shape encoding $\bar{\mathbf{z}} \in \mathbb{R}^m$ (e.g., can be obtained by using a fixed \mathbf{z} for all instances l during training or simply as the mean of $\{\mathbf{z}_l\}_l$). We initialize the shape code for the new instance with $\bar{\mathbf{z}}$ and optimize it using \mathcal{F} and \mathcal{I} and the same error function as before:

$$\begin{aligned} \min_{\mathbf{z}} & \frac{\alpha}{|\mathcal{F}|} \sum_{(\mathbf{p}, \boldsymbol{\eta}, d) \in \mathcal{F}} |\phi(d + \mathbf{p}^\top \boldsymbol{\eta}) - q_\theta(\mathbf{p}, \boldsymbol{\eta}, \mathbf{z})|^p \\ & + \frac{\beta}{|\mathcal{I}|} \sum_{(\mathbf{p}, \boldsymbol{\eta}, d) \in \mathcal{I}} r(\phi(\infty) - q_\theta(\mathbf{p}, \boldsymbol{\eta}, \mathbf{z}))^p + \sigma \|\mathbf{z}\|_p^p. \end{aligned} \quad (12)$$

The optimized latent shape code \mathbf{z}^* captures all geometric information about the object and can be used to synthesize novel distance views $h(\mathbf{p}, \boldsymbol{\eta}) = \phi^{-1}(\min\{q_\theta(\mathbf{p}, \boldsymbol{\eta}, \mathbf{z}^*), \phi(\infty)\}) - \mathbf{p}^\top \boldsymbol{\eta}$ from any point \mathbf{p} in any viewing direction $\boldsymbol{\eta}$.

4.5. Multi-view Consistency

Proposition 1 reduces the input dimension of an SDDF function $h(\mathbf{p}, \boldsymbol{\eta})$ from $2n - 1$ to $2n - 2$. To model 3D

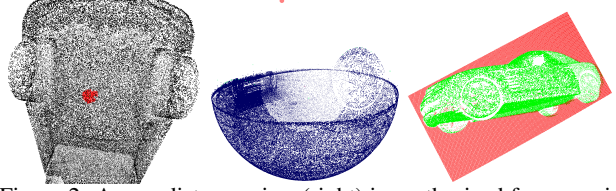


Figure 2. A new distance view (right) is synthesized from a point cloud \mathcal{P}_l (left) by deciding whether each point \mathbf{q} (left, red) is visible from the new view $\hat{\mathbf{p}}$. The point cloud is projected on a sphere around \mathbf{q} (middle) to judge the visibility from $\hat{\mathbf{p}}$ (middle, red).

shape, we need to represent a 4D SDDF function. In contrast, an SDF model [32] has a 3D input, which may even be reduced to a 2D surface using an Eikonal constraint [11]. Hence, training a multi-view consistent SDDF model might require a larger data set with distance measurements from many positions \mathbf{p} and directions $\boldsymbol{\eta}$. To reduce the necessary data, we develop an approach to synthesize additional data from the initial training set $\mathcal{D}_l := \{(\mathbf{p}_{i,l}, \boldsymbol{\eta}_{i,l}, d_{i,l})\}_i$. Given an arbitrary position $\hat{\mathbf{p}} \in \mathbb{R}^n$, we describe to how to synthesize both finite and infinite (no surface hit) distance measurements \hat{d} along different view rays $\hat{\boldsymbol{\eta}}$ originating at $\hat{\mathbf{p}}$. Let $\mathcal{P}_l := \{\mathbf{p} + d\boldsymbol{\eta} \mid (\mathbf{p}, \boldsymbol{\eta}, d) \in \mathcal{D}_l, d < \infty\}$ be a point cloud representation of the training data.

Infinite Ray Synthesis: To synthesize infinite rays, we project the point cloud \mathcal{P}_l to the desired image frame and select the directions $\hat{\boldsymbol{\eta}}$ of all pixels that do not contain a projected point. These directions correspond to views with infinite distance. The points may be inflated with a finite radius to handle sparse point cloud data.

Finite Ray Synthesis: If a point $\mathbf{q} \in \mathcal{P}_l$ is observable from $\hat{\mathbf{p}}$, we can obtain a synthetic measurement with distance $\hat{d} = \|\mathbf{q} - \hat{\mathbf{p}}\|_2$ in direction $\hat{\boldsymbol{\eta}} = \frac{1}{\hat{d}}(\mathbf{q} - \hat{\mathbf{p}})$. The challenge is to decide which points in \mathcal{P}_l are visible from $\hat{\mathbf{p}}$. For $\mathbf{q} \in \mathcal{P}_l$, let \mathbf{p} be the start point of the ray that observed \mathbf{q} originally. We know that \mathbf{q} is observable from \mathbf{p} . In contrast, for all $\mathbf{u} \in \mathcal{P}_l \setminus \{\mathbf{q}\}$ and all $\epsilon > 0$, \mathbf{q} is not observable from $\mathbf{u} - \epsilon(\mathbf{q} - \mathbf{u})$, since \mathbf{u} is in the way. Hence, \mathbf{q} is observable when we look at it in the direction $\frac{\mathbf{q} - \mathbf{p}}{\|\mathbf{q} - \mathbf{p}\|_2}$ and unobservable in the direction $\frac{\mathbf{q} - \mathbf{u}}{\|\mathbf{q} - \mathbf{u}\|_2}$ for all $\mathbf{u} \in \mathcal{P}_l \setminus \{\mathbf{q}\}$. For convenience of representation, translate all points such that \mathbf{q} is at the origin, project all points on a unit sphere around the origin, and rotate all of the points such that \mathbf{p} maps to $\mathbf{e}_3 = [0, 0, 1]^\top$. Formally, this can be achieved with the transformation:

$$T_{\mathbf{q}}(\mathbf{x}) := \begin{cases} [0, 0, 0]^\top, & \text{if } \mathbf{x} = \mathbf{q}, \\ \mathbf{R}_{\boldsymbol{\eta}} \frac{\mathbf{x} - \mathbf{q}}{\|\mathbf{x} - \mathbf{q}\|_2}, & \text{otherwise,} \end{cases} \quad (13)$$

where $\boldsymbol{\eta} = \frac{\mathbf{p} - \mathbf{q}}{\|\mathbf{p} - \mathbf{q}\|_2}$. To decide whether \mathbf{q} is observable from $\hat{\mathbf{p}}$, equivalently we should decide whether the origin is observable from $T_{\mathbf{q}}(\hat{\mathbf{p}})$. Let $\mathcal{P}_{\mathbf{q}} := T_{\mathbf{q}}(\mathcal{P}_l \setminus \{\mathbf{q}\})$. The origin is observable from \mathbf{e}_3 and a region around it and unobservable from all $\mathbf{u} \in \mathcal{P}_{\mathbf{q}}$. See Fig. 2 for an illustration.

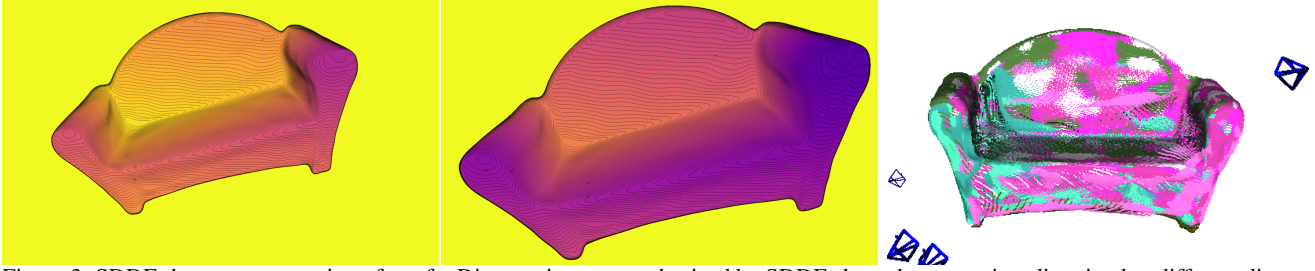


Figure 3. SDDF shape representation of a sofa. Distance images synthesized by SDDF along the same view direction but different distance from the object are shown (left, middle). Point clouds synthesized from arbitrary camera views are multi-view consistent (right).

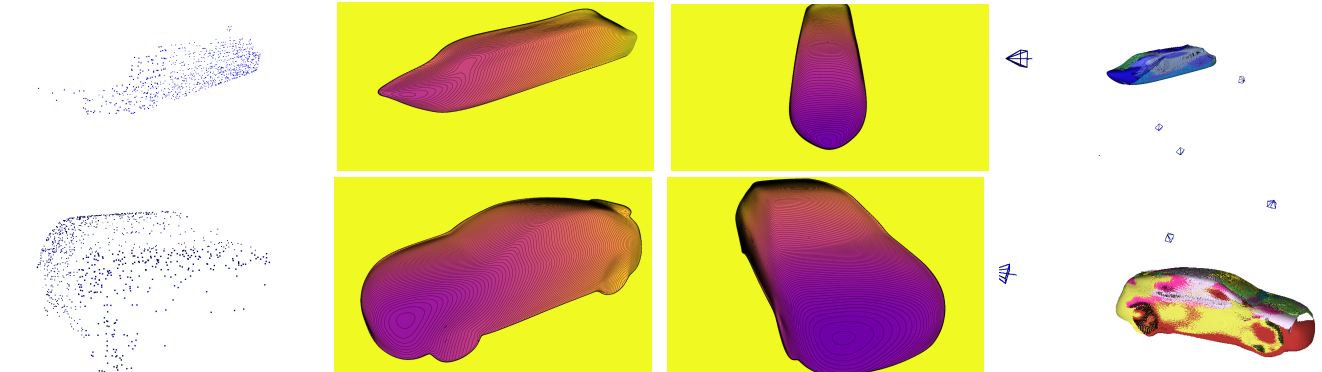


Figure 4. SDDF shape completion using distance measurements (first column) from unseen boat (first row) and car (second row) instances. The trained SDDF model can synthesize novel distance views (second and third columns) or point clouds from arbitrary camera views which are multi-view consistent (fourth column).

Spherical Convex Hull: We approximate the region of points around e_3 that can observe the origin. The vertices adjacent to e_3 in the convex hull of $\mathcal{P}_q \cup \{e_3\}$ represent the boundary. We sort the boundary points based on their azimuth so that the geodesic among them represents the boundary. The origin is observable from the part of sphere that contains the e_3 . We provide a lemma that allows the convex hull computation to be performed in 2D.

Lemma 5. *Let \mathcal{P} be a set of points on the unit sphere. The boundary points of \mathcal{P} with respect to e_3 are points that are adjacent vertices to e_3 in the convex hull of $\mathcal{P} \cup \{e_3\}$. Let m be a function that maps a point on the unit sphere to the plane $z = 0$ with center e_3 , i.e., $m([x, y, z]^\top) := [\frac{x}{1-z}, \frac{y}{1-z}]^\top$. A point $\mathbf{u} \in \mathcal{P}$ is a boundary point if and only if $m(\mathbf{u})$ is a vertex of the convex hull of $m(\mathcal{P})$.*

Proof. See the Supplementary Material. \square

To accelerate the convex hull computation further, we propose an approximation using discretization. We discretize the azimuth of the sphere into N segments. Let $E_i = \max\{el(\mathbf{u}) \mid \mathbf{u} \in \mathcal{P}_q, az(\mathbf{u}) \in [\frac{2\pi i}{N}, \frac{2\pi(i+1)}{N}]\}$, $0 \leq i < N$ be the maximum elevation of points in \mathcal{P}_q with azimuth in $[\frac{2\pi i}{N}, \frac{2\pi(i+1)}{N}]$. Then, let i determine the interval $[\frac{2\pi i}{N}, \frac{2\pi(i+1)}{N}]$ that contains the azimuth of $T_q(\hat{\mathbf{p}})$. We consider \mathbf{q} observable from $\hat{\mathbf{p}}$ if the elevation of $T_q(\hat{\mathbf{p}})$ is larger than E_i . In the experiments, we accelerate the computation further by sub-sampling \mathcal{P}_q .

5. Evaluation

This section presents qualitative and quantitative evaluation of the SDDF model. Sec. 5.1 presents results for single-instance shape modeling in comparison to the deep geometric prior (DGP) model [52]. Sec. 5.2 applies the SDDF model to a class of shapes, demonstrating shape completion from a single distance view and shape interpolation between different instances. The accuracy of SDDF for shape completion is compared against the decoder-only deep SDF model, IGR [11]. Both our model and IGR capture structural constraints for SDDF and SDF, respectively, making a quantitative comparison interesting. We also compare the results against a group of category-level shape modeling methods [12, 22, 48, 54, 58, 62] that utilize point-cloud data. Finally, we present SDDF shape interpolation results to demonstrate that our model captures the latent space of an object category shape continuously and meaningfully.

Network Architecture: We use an autoencoder with 16 layers, 512 hidden units per layer, and a skip connection from the input to layers 4, 8, 12 to represent the SDDF model $q_\theta(\mathbf{p}, \boldsymbol{\eta}, \mathbf{z})$ introduced in Sec. 4.4. The dimension of the latent shape code \mathbf{z} is set to 256 for category-level shape completion and interpolation and to 0 for single instance shape modeling.

Data Preparation: We use the ShapeNet dataset [4]. Distance images with resolution 512×512 are generated as training data from 8 camera views facing the object from az-

Table 1. Quantitative comparison between DGP [52] and SDDF with exact (SDDF (conv)) and approximate (SDDF (disc)) convex hull data augmentation on 5 object instances from ShapeNet [4]. At test time, the metrics from [26] are computed after the reconstructed meshes are normalized to a unit-length bounding box.

Class	Method	Chamfer- L_2	Chamfer- L_1	Completeness	Accuracy
Truck	SDDF (conv)	3.918e-05	3.475e-03	3.077e-03	3.874e-03
	SDDF (disc)	4.421e-05	3.681e-03	3.251e-03	4.111e-03
	DGP	8.842e-05	7.388e-03	6.842e-03	7.935e-03
Airplane	SDDF (conv)	3.088e-05	2.135e-03	1.713e-03	2.557e-03
	SDDF (disc)	2.332e-05	2.741e-03	2.077e-03	3.406e-03
	DGP	4.900e-05	5.141e-03	4.512e-03	5.770e-03
Sofa	SDDF (conv)	1.562e-05	2.428e-03	1.725e-03	3.130e-03
	SDDF (disc)	2.563e-05	2.610e-03	1.767e-03	3.454e-03
	DGP	18.822e-05	10.747e-03	9.546e-03	11.949e-03
Boat	SDDF (conv)	0.425e-05	1.725e-03	1.446e-03	2.005e-03
	SDDF (disc)	0.489e-05	1.778e-03	1.481e-03	2.075e-03
	DGP	2.399e-05	4.015e-03	3.848e-03	4.182e-03
Car	SDDF (conv)	2.889e-05	2.892e-03	2.858e-03	2.925e-03
	SDDF (disc)	2.765e-05	2.921e-03	2.824e-03	3.019e-03
	DGP	5.988e-05	5.927e-03	5.809e-03	6.046e-03

Table 2. Comparison between SDDF and IGR [11], over 5 classes from ShapeNet [4], using the metrics from [26]. The metrics are computed after the reconstructed meshes are normalized in a unit-length bounding box. Two versions of IGR are evaluated: IGR(1), using the same test points as SDDF, and IGR(2), producing a uniform point cloud from the reconstructed mesh.

Class	Method	Chamfer- L_2	Chamfer- L_1	Completeness	Accuracy
Car	SDDF	2.688e-04	8.365e-03	7.833e-03	8.897e-03
	IGR(1)	37.873e-04	39.682e-03	15.971e-03	63.394e-03
	IGR(2)	27.165e-04	30.465e-03	11.291e-03	49.639e-03
Airplane	SDDF	3.539e-04	7.735e-03	6.790e-03	8.680e-03
	IGR(1)	182.028e-04	89.677e-03	21.411e-03	157.942e-03
	IGR(2)	139.607e-04	70.804e-03	10.752e-03	130.856e-03
Watercraft	SDDF	7.869e-04	12.762e-03	10.772e-03	14.752e-03
	IGR(1)	72.551e-04	55.594e-03	25.620e-03	85.567e-03
	IGR(2)	69.437e-04	52.774e-03	22.409e-03	83.139e-03
Sofa	SDDF	3.952e-04	12.245e-03	10.940e-03	13.551e-03
	IGR(1)	119.493e-04	71.506e-03	40.964e-03	102.048e-03
	IGR(2)	114.114e-04	67.189e-03	33.903e-03	100.475e-03
Display	SDDF	9.318e-04	17.089e-03	14.051e-03	20.127e-03
	IGR(1)	93.326e-04	53.326e-03	35.082e-03	71.571e-03
	IGR(2)	86.551e-04	53.734e-03	36.470e-03	70.998e-03

$\text{imath } \frac{k\pi}{4}$ and elevation $\frac{(-1)^k\pi}{4}$ for $k = 0, \dots, 7$ on a sphere. Each distance image is subsampled to contain at most $100k$ finite and $100k$ infinite distance measurements. Both DGP and IGR were trained using the point cloud obtained from all points with finite distance measurements and augmented with normals obtained using the method of [66]. The results of the remaining baseline methods [12, 22, 48, 54, 58, 62] were obtained from the GRNet paper [54].

5.1. Geometric Model Evaluation

We first evaluate the performance of our SDDF model and DGP [52] for single-instance shape reconstruction using 5 objects from ShapeNet [4]. The models are trained using point cloud data from 8 views described above. The data is augmented with normals for DGP and the DGP radius is set to guarantee at least 128 patches for each ob-

Table 3. Quantitative comparison between SDDF and several baseline methods reported in GRNet [54], over 4 classes from ShapeNet [4]. The errors are scaled by $\times 10^{-3}$.

Class	Metric	Car	Airplane	Watercraft	Sofa
AtlasNet	Chamfer- L_2	0.3237	0.1753	0.4177	0.5990
	Chamfer- L_1	10.105	6.366	10.607	12.990
PCN	Chamfer- L_2	0.2445	0.1400	0.4062	0.5129
	Chamfer- L_1	8.696	5.502	9.665	11.676
FoldingNet	Chamfer- L_2	0.4676	0.3151	0.7325	0.8895
	Chamfer- L_1	12.611	9.491	14.987	15.969
TopNet	Chamfer- L_2	0.3513	0.2152	0.4359	0.6949
	Chamfer- L_1	10.898	7.614	11.124	14.779
MSN	Chamfer- L_2	0.4711	0.1543	0.3853	0.5894
	Chamfer- L_1	10.776	5.596	9.485	11.895
GRNet	Chamfer- L_2	0.2752	0.1531	0.2122	0.3613
	Chamfer- L_1	9.447	6.450	8.039	10.512
SDDF	Chamfer- L_2	0.17351	0.26172	0.39942	0.23767
	Chamfer- L_1	8.31331	5.90701	9.80779	9.8593

ject. SDDF is trained with learning rate 0.005 that decreases every $1k$ epoch by factor of 0.5 for $10k$ epochs using additional synthesized data with exact (SDDF (conv)) and discretized (SDDF (disc)) convex hull computation (see Sec. 4.5). The results are presented in Table 1.

Given the trained SDDF model, we can generate a distance image at an arbitrary view by calculating an SDDF prediction for the rays corresponding to each pixel in the desired image. To visualize the learned model, we choose camera locations facing the object and show the predictions in Fig. 3. All generated distance images recognize the object shape and free space precisely. By inspecting the distance level sets, we can also conclude that the SDDF model successfully captures the shape details. The images get brighter as the view moves further away from the object because the measured distances at each pixel increase. On the other hand, the level sets in the distant view remain parallel to the close-up view. The two-view comparison shows that the directional condition of the SDDF model in (2) holds.

5.2. Latent Space Learning and Shape Completion

In this section, we explore the capability of our method to represent a whole category of object shapes.

Shape Completion: First, we focus on recognizing the shape of an unseen instance based on a single distance image or point cloud observation. Given a trained category auto-decoder q_θ , we optimize the latent shape code $z \in \mathbb{R}^{256}$ for the unseen instance using (12). We train SDDF and IGR [11] for 1000 epochs, with 2000 random samples, and with learning rate 0.0005, 0.0001 for the network weights and latent code weights. The learning rate decreases by factor of 2 every 500 epochs for IGR (as suggested in the paper [11]) and every 200 epochs for SDDF. At test time, for each instance we take a distance image from one view and down sample it such that we have 1000 finite

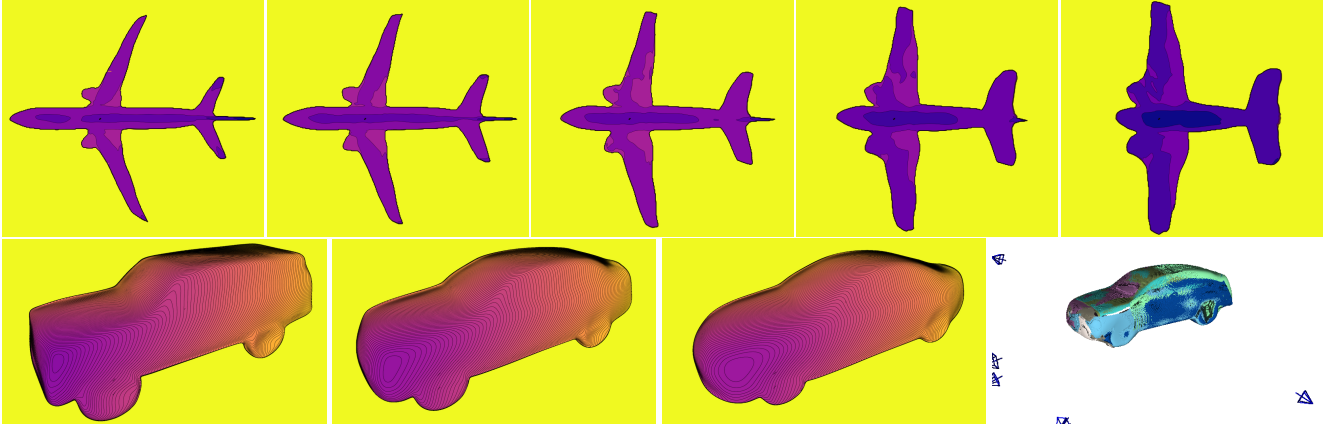


Figure 5. SDDF shape interpolation between two instances. The left-most and right-most column in the first row show the SDDF output from the same view for two different airplane instances from the training set. The three columns in the middle are generated by using a weighted average of the latent codes of the left-most and right-most instances as an input to the SDDF network. In each row, from left to right, the latent code weights with respect to the left-most instance are 1, 0.75, 0.5, 0.25, 0, respectively. Note how the shapes transform smoothly from the left-most to the right-most instance with intermediate shapes looking like valid airplanes. The second row shows interpolation (in column 2) between two learned car shapes (in columns 1, 3). The last column shows the point cloud reconstruction of the interpolated car instance from several different views.

rays and 1000 infinite rays. We use this data for our method and the associated point cloud, augmented with normals, for IGR to optimize the latent code. The shape reconstruction accuracy is evaluated at 8 views different from the one used to obtain first distance image. The SDDF model can directly generate point clouds for these query views, as shown in Fig. 4. To obtain point cloud predictions from IGR, we used the Marching cubes algorithm [29] to extract a mesh from the predicted SDF and used the same 8 views to generate noiseless point clouds (IGR(1)). Additionally, we generated a uniform point cloud from the IGR mesh (IGR(2)) and compared it with ground truth point cloud. The results are presented in Table 2.

We also compare the SDDF reconstruction accuracy versus GRNet [54], AtlasNet [12], PCN [62], FoldingNet [58], TopNet [48], and MSN [22] in Table 3. The reconstructed objects are not normalized to a unit-length bounding box in these experiments since the baseline methods did not do this. Our method learns a higher dimensional representation than these methods, so it needs more training data. The training data used by the baseline methods was insufficient to obtain reliable convex hull approximation results. To make the comparison as fair as possible, our method was trained on the same categories with the same train/test splits and was evaluated at view rays that collide with the points used for testing of the baseline methods.

Shape Interpolation: Finally, we demonstrate that the SDDF model represents the latent shape space of an object category continuously and meaningfully. Fig. 17 presents results for linear interpolation between the latent shape codes of two object instances from the training set.

5.3. Limitations

Our method models the distance to an object from any location and orientation. This comes at a price of increased dimension compared to SDF models that only represent the object surface. Our result in Proposition 1 reduces the SDDF input dimension from 5 to 4 for modeling 3D shapes. However, our method still requires more training data compared to SDF models to achieve multi-view consistency. We introduced a data augmentation technique to synthesize data from novel views and alleviate the data requirements. This requires a spherical convex hull computation, which increases the training time, but we introduced a reasonable approximation method using discretization. Our method currently does not utilize additional geometric information such as normals, which may improve the performance. It also cannot currently be trained from RGB images only due to its reliance on distance data.

6. Conclusion

This work proposed a signed directional distance function as an implicit representation of object shape. Any valid SDDF was shown to satisfy a gradient condition, which should be respected by neural network approximations. We designed an auto-decoder model that guarantees the gradient condition by construction and can be trained efficiently without 3D supervision using distance measurements from depth camera or Lidar sensors. The SDDF model offers a promising approach for scene modeling in applications requiring efficient visibility or collision checking. Future work will focus on extending the SDDF model to capture texture, color, and lighting and represent complete scenes.

References

- [1] Panos Achlioptas, Olga Diamanti, Ioannis Mitliagkas, and Leonidas Guibas. Learning representations and generative models for 3D point clouds. In *International Conference on Machine Learning (ICML)*, pages 40–49, 2018. [2](#)
- [2] J. Ángel Cid and F. Adrián F. Tojo. A Lipschitz condition along a transversal foliation implies local uniqueness for ODEs. *Electronic Journal of Qualitative Theory of Differential Equations*, *arXiv:1801.01724*, 36(4):1–13, 2018. [3](#)
- [3] OK-C Au, Chiew-Lan Tai, Ligang Liu, and Hongbo Fu. Dual Laplacian Editing for Meshes. *IEEE Transactions on Visualization and Computer Graphics*, 12(3):386–395, 2006. [2](#)
- [4] Angel X Chang, Thomas Funkhouser, Leonidas Guibas, Pat Hanrahan, Qixing Huang, Zimo Li, Silvio Savarese, Manolis Savva, Shuran Song, Hao Su, Jianxiong Xiao, Li Yi, and Fisher Yu. ShapeNet: An Information-Rich 3D Model Repository. *arXiv:1512.03012*, 2015. [2](#), [6](#), [7](#), [20](#)
- [5] Anpei Chen, Zexiang Xu, Fuqiang Zhao, Xiaoshuai Zhang, Fanbo Xiang, Jingyi Yu, and Hao Su. MVSNeRF: Fast Generalizable Radiance Field Reconstruction From Multi-View Stereo. In *IEEE/CVF International Conference on Computer Vision (ICCV)*, pages 14124–14133, 2021. [3](#)
- [6] Zhiqin Chen and Hao Zhang. Learning implicit fields for generative shape modeling. In *IEEE/CVF Conference on Computer Vision and Pattern Recognition (CVPR)*, pages 5939–5948, 2019. [2](#)
- [7] Christopher B Choy, Danfei Xu, JunYoung Gwak, Kevin Chen, and Silvio Savarese. 3d-r2n2: A unified approach for single and multi-view 3d object reconstruction. In *European Conference on Computer Vision (ECCV)*, pages 628–644. Springer, 2016. [2](#)
- [8] Brian Curless and Marc Levoy. A volumetric method for building complex models from range images. In *Conference on Computer Graphics and Interactive Techniques*, pages 303–312, 1996. [2](#)
- [9] Lin Gao, Yu-Kun Lai, Jie Yang, Zhang Ling-Xiao, Shihong Xia, and Leif Kobbelt. Sparse data driven mesh deformation. *IEEE Transactions on Visualization and Computer Graphics*, 27(3):2085–2100, 2021. [2](#)
- [10] Kyle Genova, Forrester Cole, Avneesh Sud, Aaron Sarna, and Thomas Funkhouser. Local deep implicit functions for 3d shape. In *IEEE/CVF Conference on Computer Vision and Pattern Recognition (CVPR)*, June 2020. [2](#)
- [11] Amos Gropp, Lior Yariv, Niv Haim, Matan Atzmon, and Yaron Lipman. Implicit Geometric Regularization for Learning Shapes. In *International Conference on Machine Learning (ICML)*, pages 3789–3799, 2020. [1](#), [2](#), [5](#), [6](#), [7](#), [12](#), [20](#)
- [12] Thibault Groueix, Matthew Fisher, Vladimir G Kim, Bryan C Russell, and Mathieu Aubry. A papier-mâché approach to learning 3d surface generation. In *IEEE/CVF Conference on Computer Vision and Pattern Recognition (CVPR)*, pages 216–224, 2018. [2](#), [6](#), [7](#), [8](#)
- [13] Luxin Han, Fei Gao, Boyu Zhou, and Shaojie Shen. Fiesta: Fast incremental euclidean distance fields for online motion planning of aerial robots. In *IEEE/RSJ Int. Conf. on Intelligent Robots and Systems*, 2019. [1](#)
- [14] Doug P Hardin, Edward B Saff, et al. Discretizing manifolds via minimum energy points. *Notices of the AMS*, 51(10):1186–1194, 2004. [12](#)
- [15] Ajay Jain, Matthew Tancik, and Pieter Abbeel. Putting nerf on a diet: Semantically consistent few-shot view synthesis. In *IEEE/CVF International Conference on Computer Vision (ICCV)*, pages 5885–5894, 2021. [3](#)
- [16] Chiyu ”Max” Jiang, Avneesh Sud, Ameesh Makadia, Jingwei Huang, Matthias Niessner, and Thomas Funkhouser. Local implicit grid representations for 3d scenes. In *IEEE/CVF Conference on Computer Vision and Pattern Recognition (CVPR)*, June 2020. [2](#)
- [17] Angjoo Kanazawa, Shubham Tulsiani, Alexei A. Efros, and Jitendra Malik. Learning category-specific mesh reconstruction from image collections. In *European Conference on Computer Vision (ECCV)*, 2018. [1](#)
- [18] Diederik P Kingma and Jimmy Ba. Adam: A method for stochastic optimization. *arXiv preprint arXiv:1412.6980*, 2014. [12](#), [20](#)
- [19] Leif Kobbelt, Swen Campagna, Jens Vorsatz, and Hans-Peter Seidel. Interactive multi-resolution modeling on arbitrary meshes. In *Conference on Computer Graphics and Interactive Techniques*, pages 105–114, 1998. [2](#)
- [20] Ruihui Li, Xianzhi Li, Chi-Wing Fu, Daniel Cohen-Or, and Pheng-Ann Heng. PU-GAN: A Point Cloud Upsampling Adversarial Network. In *IEEE/CVF International Conference on Computer Vision (ICCV)*, pages 7203–7212, 2019. [2](#)
- [21] Chen-Hsuan Lin, Chaoyang Wang, and Simon Lucey. SDF-SRN: Learning Signed Distance 3D Object Reconstruction from Static Images. In *Advances in Neural Information Processing Systems (NeurIPS)*, 2020. [2](#)
- [22] Minghua Liu, Lu Sheng, Sheng Yang, Jing Shao, and Shi-Min Hu. Morphing and sampling network for dense point cloud completion. In *Proceedings of the AAAI conference on artificial intelligence*, volume 34, pages 11596–11603, 2020. [2](#), [6](#), [7](#), [8](#)
- [23] Haggai Maron, Meirav Galun, Noam Aigerman, Miri Trope, Nadav Dym, Ersin Yumer, Vladimir G Kim, and Yaron Lipman. Convolutional neural networks on surfaces via seamless toric covers. *ACM Trans. Graph.*, 36(4):71–1, 2017. [2](#)
- [24] Ricardo Martin-Brualla, Noha Radwan, Mehdi SM Sajjadi, Jonathan T Barron, Alexey Dosovitskiy, and Daniel Duckworth. Nerf in the wild: Neural radiance fields for unconstrained photo collections. *arXiv preprint arXiv:2008.02268*, 2020. [2](#)
- [25] Matthew Matl. Pyrender. <https://github.com/mmatl/pyrender>, 2019. [12](#)
- [26] Lars Mescheder, Michael Oechsle, Michael Niemeyer, Sebastian Nowozin, and Andreas Geiger. Occupancy networks: Learning 3D reconstruction in function space. In *IEEE/CVF Conference on Computer Vision and Pattern Recognition (CVPR)*, pages 4460–4470, 2019. [1](#), [2](#), [7](#)
- [27] Ben Mildenhall, Pratul P Srinivasan, Matthew Tancik, Jonathan T Barron, Ravi Ramamoorthi, and Ren Ng. Nerf: Representing scenes as neural radiance fields for view synthesis. In *European Conference on Computer Vision*, pages 405–421. Springer, 2020. [1](#), [2](#)

- [28] Jiteng Mu, Weichao Qiu, Adam Kortylewski, Alan Yuille, Nuno Vasconcelos, and Xiaolong Wang. A-SDF: Learning Disentangled Signed Distance Functions for Articulated Shape Representation. In *IEEE/CVF International Conference on Computer Vision (ICCV)*, 2021. 2
- [29] Timothy S Newman and Hong Yi. A survey of the marching cubes algorithm. *Computers & Graphics*, 30(5):854–879, 2006. 8
- [30] Lachlan Nicholson, Michael Milford, and Niko Sünderhauf. Quadriclam: Dual quadrics from object detections as landmarks in object-oriented slam. *IEEE Robotics and Automation Letters*, 4(1):1–8, 2018. 2
- [31] Michael Niemeyer, Lars Mescheder, Michael Oechsle, and Andreas Geiger. Differentiable volumetric rendering: Learning implicit 3D representations without 3D supervision. In *Proceedings of the IEEE/CVF Conference on Computer Vision and Pattern Recognition*, pages 3504–3515, 2020. 2
- [32] Jeong Joon Park, Peter Florence, Julian Straub, Richard Newcombe, and Steven Lovegrove. DeepSDF: Learning continuous signed distance functions for shape representation. In *IEEE/CVF Conference on Computer Vision and Pattern Recognition (CVPR)*, pages 165–174, 2019. 1, 2, 5
- [33] Despoina Paschalidou, Ali Osman Ulusoy, and Andreas Geiger. Superquadrics revisited: Learning 3d shape parsing beyond cuboids. In *IEEE/CVF Conference on Computer Vision and Pattern Recognition (CVPR)*, 2019. 2
- [34] Adam Paszke, Sam Gross, Soumith Chintala, Gregory Chanan, Edward Yang, Zachary DeVito, Zeming Lin, Alban Desmaison, Luca Antiga, and Adam Lerer. Automatic differentiation in pytorch. 2017. 12, 20
- [35] Charles R Qi, Hao Su, Kaichun Mo, and Leonidas J Guibas. Pointnet: Deep learning on point sets for 3d classification and segmentation. In *IEEE Conference on Computer Vision and Pattern Recognition (CVPR)*, pages 652–660, 2017. 2
- [36] Nikhila Ravi, Jeremy Reizenstein, David Novotny, Taylor Gordon, Wan-Yen Lo, Justin Johnson, and Georgia Gkioxari. Accelerating 3d deep learning with pytorch3d. *arXiv:2007.08501*, 2020. 20
- [37] Gernot Riegler, Ali Osman Ulusoy, and Andreas Geiger. Octnet: Learning deep 3d representations at high resolutions. In *Proceedings of the IEEE conference on computer vision and pattern recognition*, pages 3577–3586, 2017. 2
- [38] Gernot Riegler, Ali Osman Ulusoy, Horst Bischof, and Andreas Geiger. Octnetfusion: Learning depth fusion from data. In *2017 International Conference on 3D Vision (3DV)*, pages 57–66. IEEE, 2017. 2
- [39] Shaul Salomon, Gideon Avigad, Alex Goldvard, and Oliver Schütze. Psa—a new scalable space partition based selection algorithm for moeas. In *EVOLVE-A Bridge between Probability, Set Oriented Numerics, and Evolutionary Computation II*, pages 137–151. Springer, 2013. 12
- [40] Katja Schwarz, Yiyi Liao, Michael Niemeyer, and Andreas Geiger. GRAF: Generative Radiance Fields for 3D-Aware Image Synthesis. In *Advances in Neural Information Processing Systems*, volume 33, pages 20154–20166, 2020. 2
- [41] Dong Wook Shu, Sung Woo Park, and Junseok Kwon. 3d point cloud generative adversarial network based on tree structured graph convolutions. In *IEEE/CVF International Conference on Computer Vision (ICCV)*, pages 3859–3868, 2019. 2
- [42] Ayan Sinha, Asim Unmesh, Qixing Huang, and Karthik Ramani. Surfnet: Generating 3d shape surfaces using deep residual networks. In *IEEE/CVF Conference on Computer Vision and Pattern Recognition (CVPR)*, pages 6040–6049, 2017. 2
- [43] Vincent Sitzmann, Julien Martel, Alexander Bergman, David Lindell, and Gordon Wetzstein. Implicit neural representations with periodic activation functions. In H. Larochelle, M. Ranzato, R. Hadsell, M. F. Balcan, and H. Lin, editors, *Advances in Neural Information Processing Systems*, volume 33, pages 7462–7473, 2020. 2
- [44] Vincent Sitzmann, Michael Zollhöfer, and Gordon Wetzstein. Scene Representation Networks: Continuous 3D-Structure-Aware Neural Scene Representations. In *Advances in Neural Information Processing Systems*, 2019. 2
- [45] Olga Sorkine, Daniel Cohen-Or, Yaron Lipman, Marc Alexa, Christian Rössl, and H-P Seidel. Laplacian surface editing. In *ACM SIGGRAPH Symposium on Geometry Processing*, pages 175–184, 2004. 2
- [46] Qingyang Tan, Lin Gao, Yu-Kun Lai, and Shihong Xia. Variational autoencoders for deforming 3d mesh models. In *Proceedings of the IEEE conference on computer vision and pattern recognition*, pages 5841–5850, 2018. 2
- [47] Maxim Tatarchenko, Alexey Dosovitskiy, and Thomas Brox. Octree generating networks: Efficient convolutional architectures for high-resolution 3d outputs. In *IEEE International Conference on Computer Vision (ICCV)*, pages 2088–2096, 2017. 2
- [48] Lyne P Tchammi, Vineet Kosaraju, Hamid RezaTofighi, Ian Reid, and Silvio Savarese. Topnet: Structural point cloud decoder. In *Proceedings of the IEEE/CVF Conference on Computer Vision and Pattern Recognition*, pages 383–392, 2019. 2, 6, 7, 8
- [49] Alex Trevithick and Bo Yang. GRF: Learning a General Radiance Field for 3D Scene Representation and Rendering. In *IEEE/CVF International Conference on Computer Vision (ICCV)*, 2021. 2
- [50] Shubham Tulsiani, Hao Su, Leonidas J Guibas, Alexei A Efros, and Jitendra Malik. Learning shape abstractions by assembling volumetric primitives. In *IEEE/CVF Conference on Computer Vision and Pattern Recognition (CVPR)*, pages 2635–2643, 2017. 1, 2
- [51] Qianqian Wang, Zhicheng Wang, Kyle Genova, Pratul Srinivasan, Howard Zhou, Jonathan T. Barron, Ricardo Martin-Brualla, Noah Snavely, and Thomas Funkhouser. IBRNet: Learning Multi-View Image-Based Rendering. In *CVPR*, 2021. 2
- [52] Francis Williams, Teseo Schneider, Claudio Silva, Denis Zorin, Joan Bruna, and Daniele Panozzo. Deep geometric prior for surface reconstruction. In *IEEE/CVF Conference on Computer Vision and Pattern Recognition (CVPR)*, 2019. 2, 6, 7, 12
- [53] Jiajun Wu, Chengkai Zhang, Tianfan Xue, William T Freeman, and Joshua B Tenenbaum. Learning a probabilistic

- latent space of object shapes via 3d generative-adversarial modeling. *arXiv preprint:1610.07584*, 2016. 2
- [54] Haozhe Xie, Hongxun Yao, Shangchen Zhou, Jiageng Mao, Shengping Zhang, and Wenxiu Sun. Grnet: Gridding residual network for dense point cloud completion. In *European Conference on Computer Vision*, pages 365–381. Springer, 2020. 2, 6, 7, 8
- [55] Qiangeng Xu, Weiyue Wang, Duygu Ceylan, Radomir Mech, and Ulrich Neumann. DISN: Deep Implicit Surface Network for High-quality Single-view 3D Reconstruction. In *Advances in Neural Information Processing Systems*, pages 492–502. 2019. 2
- [56] Guandao Yang, Xun Huang, Zekun Hao, Ming-Yu Liu, Serge Belongie, and Bharath Hariharan. Pointflow: 3D point cloud generation with continuous normalizing flows. In *IEEE/CVF International Conference on Computer Vision (ICCV)*, pages 4541–4550, 2019. 2
- [57] Shichao Yang and Sebastian Scherer. Cubeslam: Monocular 3-d object slam. *IEEE Transactions on Robotics*, 35(4):925–938, 2019. 2
- [58] Yaoqing Yang, Chen Feng, Yiru Shen, and Dong Tian. Foldingnet: Point cloud auto-encoder via deep grid deformation. In *Proceedings of the IEEE Conference on Computer Vision and Pattern Recognition*, pages 206–215, 2018. 2, 6, 7, 8
- [59] Lior Yariv, Yoni Kasten, Dror Moran, Meirav Galun, Matan Atzmon, Basri Ronen, and Yaron Lipman. Multiview Neural Surface Reconstruction by Disentangling Geometry and Appearance. In *Advances in Neural Information Processing Systems*, volume 33, pages 2492–2502, 2020. 2
- [60] Yikuan Yu, Zitian Huang, Fei Li, Haodong Zhang, and Xinyi Le. Point Encoder GAN: A deep learning model for 3D point cloud inpainting. *Neurocomputing*, 384:192–199, 2020. 2
- [61] Yizhou Yu, Kun Zhou, Dong Xu, Xiaohan Shi, Hujun Bao, Baining Guo, and Heung-Yeung Shum. Mesh editing with poisson-based gradient field manipulation. In *ACM SIG-GRAPH*, pages 644–651. 2004. 2
- [62] Wentao Yuan, Tejas Khot, David Held, Christoph Mertz, and Martial Hebert. Pcn: Point completion network. In *2018 International Conference on 3D Vision (3DV)*, pages 728–737. IEEE, 2018. 2, 6, 7, 8
- [63] Andy Zeng, Shuran Song, Matthias Nießner, Matthew Fisher, Jianxiong Xiao, and Thomas Funkhouser. 3dmatch: Learning local geometric descriptors from rgb-d reconstructions. In *IEEE/CVF Conference on Computer Vision and Pattern Recognition (CVPR)*, pages 1802–1811, 2017. 2
- [64] Jingyang Zhang, Yao Yao, and Long Quan. Learning Signed Distance Field for Multi-View Surface Reconstruction. In *IEEE/CVF International Conference on Computer Vision (ICCV)*, pages 6525–6534, 2021. 2
- [65] Kun Zhou, John Michael Snyder, Xinguo Liu, Baining Guo, and Heung-yeung Shum. Large mesh deformation using the volumetric graph laplacian, Oct. 23 2007. US Patent 7,286,127. 2
- [66] Qian-Yi Zhou, Jaesik Park, and Vladlen Koltun. Open3D: A modern library for 3D data processing. *arXiv:1801.09847*, 2018. 7
- [67] E. Zobeidi, A. Koppel, and N. Atanasov. Dense Incremental Metric-Semantic Mapping via Sparse Gaussian Process Regression. In *IEEE/RSJ International Conference on Intelligent Robots and Systems (IROS)*, 2020. 2

7. Supplementary Material

7.1. Network Architecture and Training Details

We present additional details about the network architecture for $q_{\theta}(\mathbf{p}, \boldsymbol{\eta}, \mathbf{z})$ and the training procedure. The results in Sec. 5 are generated with an 16 layer fully connected network with 512 hidden units per layer and a skip connection from the input to layers 4, 8, 12 (every 4 layers). We use a soft-plus activation function $\frac{1}{\beta} \ln(1 + \exp(\beta x))$ with $\beta = 100$. The inputs are positions $\mathbf{p} \in \mathbb{R}^3$, view direction $\boldsymbol{\eta} \in S^2$, and latent code $\mathbf{z} \in \mathbb{R}^{256}$. The third component of $\boldsymbol{\eta}$ (c in Lemma 3) may be very close to -1 . To avoid numerical problems, we let $\boldsymbol{\eta} = [\sin(\theta) \cos(\phi), \sin(\theta) \sin(\phi), \cos(\theta)]^{\top}$. Using $s_{\theta} := \sin(\theta)$, $c_{\theta} := \cos(\theta)$, $s_{\phi} := \sin(\phi)$, $c_{\phi} := \cos(\phi)$, and applying the fact that $\frac{s_{\theta}^2}{1+c_{\theta}} = \frac{1-c_{\theta}^2}{1+c_{\theta}} = 1 - c_{\theta}$, the rotation matrix $\mathbf{R}_{\boldsymbol{\eta}}$ in Lemma 3 used to map $\boldsymbol{\eta}$ to the standard basis vector \mathbf{e}_3 becomes:

$$\mathbf{R}_{\boldsymbol{\eta}} = \begin{bmatrix} 1 - (1 - c_{\theta})c_{\phi}^2 & -(1 - c_{\theta})s_{\phi}c_{\phi} & -s_{\theta}c_{\phi} \\ -(1 - c_{\theta})s_{\phi}c_{\phi} & 1 - (1 - c_{\theta})s_{\phi}^2 & -s_{\theta}s_{\phi} \\ s_{\theta}c_{\phi} & s_{\theta}s_{\phi} & c_{\theta} \end{bmatrix}.$$

Using the dimension reduction in Proposition 1, the final network inputs are $\mathbf{P}\mathbf{R}_{\boldsymbol{\eta}}\mathbf{p} \in \mathbb{R}^2$, $\boldsymbol{\eta} \in S^2$, and $\mathbf{z} \in \mathbb{R}^{256}$.

All experiments are done on a single GTX 1080 Ti GPU with the PyTorch deep learning framework [34] and the ADAM optimizer [18]. For single shape estimation, the network is trained with initial learning rate of 0.005, decreasing by a factor of 2 every 1000 steps for $10k$ iterations. In each iteration, we pick a batch of $100k$ samples randomly from the synthesized training data and use $\alpha = 1$, $\beta = 0.5$, $\gamma = 0$, $p = 1$, $r(x) = \max\{0, x\}$ in the error function in (10). For category-level shape estimation, the network is trained with initial learning rate of 0.0005 for the network parameters $\boldsymbol{\theta}$ and 0.0001 for latent code \mathbf{z} , both decreasing by a factor of 2 every 200 steps for $1k$ iterations. In each iteration, for each object we pick a batch of $2k$ samples randomly from the union of the synthesized and original samples. We use $\alpha = 1$, $\beta = 1$, $p = 1$, $r(x) = \max\{0, x\}$, $\sigma = 0.001$ and Euclidean norm regularization $\|\mathbf{z}\|_2^2$ for the latent shape code in the error function (12).

To train the IGR network [11], for each object we picked a batch of $2k$ samples randomly from the original point cloud and augmented them with normals. Note that for our method we pick a total of $2k$ samples for each object, including the original data and synthesized data as well as finite rays and infinite rays. We use the default training parameters for IGR as provided in the open-source implementation [11]. The only parameter we adjusted was the initial learning rate because there was a discrepancy between the open source code and the IGR paper. We chose the setting that provided better results, namely initial learning rate of 0.0005 for network parameters $\boldsymbol{\theta}$ and 0.0001 for latent code

\mathbf{z} , both decreasing by a factor of 2 every 500 steps for $1k$ iterations.

We use the default training parameters for the DGP network [52], except increasing the upsamples-per-patch parameter from 8 to 20 and adjusting the radius parameter to guarantee at least 128 patches for each object.

To produce training data for the category-level experiments, we normalize each instance to a unit box and generate 8 distance images with resolution 512×512 using PyRenderer [25]. Each distance image is subsampled to have at most 12500 infinite rays and 12500 finite rays. Hence, there are at most $100k$ finite and $100k$ infinite rays for each object. To accelerate the data augmentation procedure, we further subsample the point cloud produced by the finite rays in each view from 12500 to 1250 points, when computing the convex hull approximation in Sec. 4.5. This provides a subsampled point cloud across all views with at most $10k$ points, which was further subsampled to $2k$ points using the diversipy python package [14, 39]. To generate synthetic data, we choose $1k$ random azimuth and elevation views on a sphere around the point cloud. Infinite rays are obtained by projecting the original point cloud (with $100k$ points) to an image plane with resolution 128×128 for each imaginary camera and selecting the unoccupied pixel directions. Finite rays are generated using the procedure described in Sec. 4.5.

Additional qualitative results for shape completion are presented in Fig. 6 and for shape interpolation in Fig. 7, Fig. 8, Fig. 9, Fig. 10.

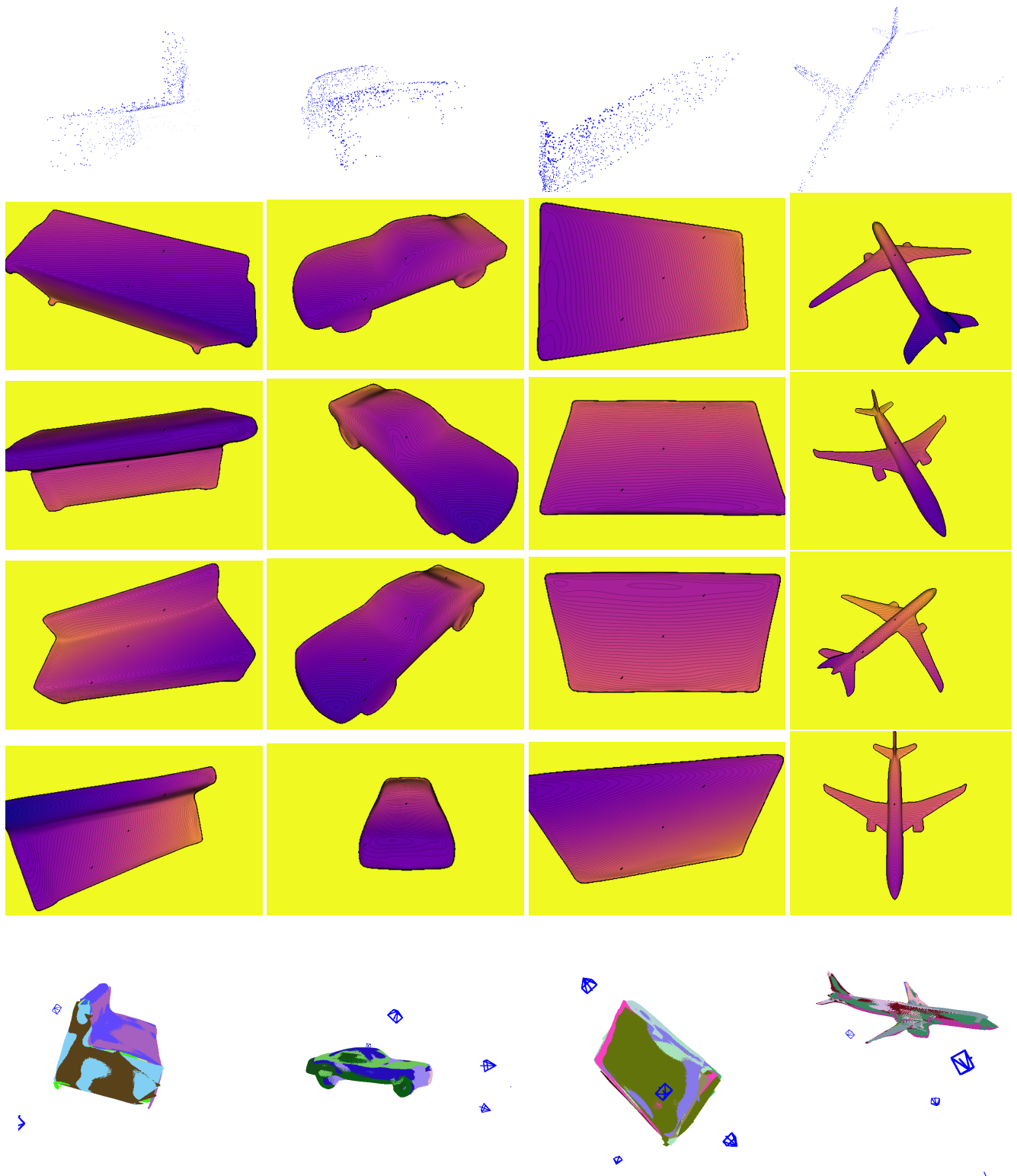


Figure 6. SDDF shape completion using $1k$ finite and $1k$ infinite rays from a single distance view and the corresponding point cloud (upper row) from an unseen object instance. After latent code optimization, the SDDF model can synthesize novel distance views (the four middle rows), and novel point clouds from arbitrary views (last row).

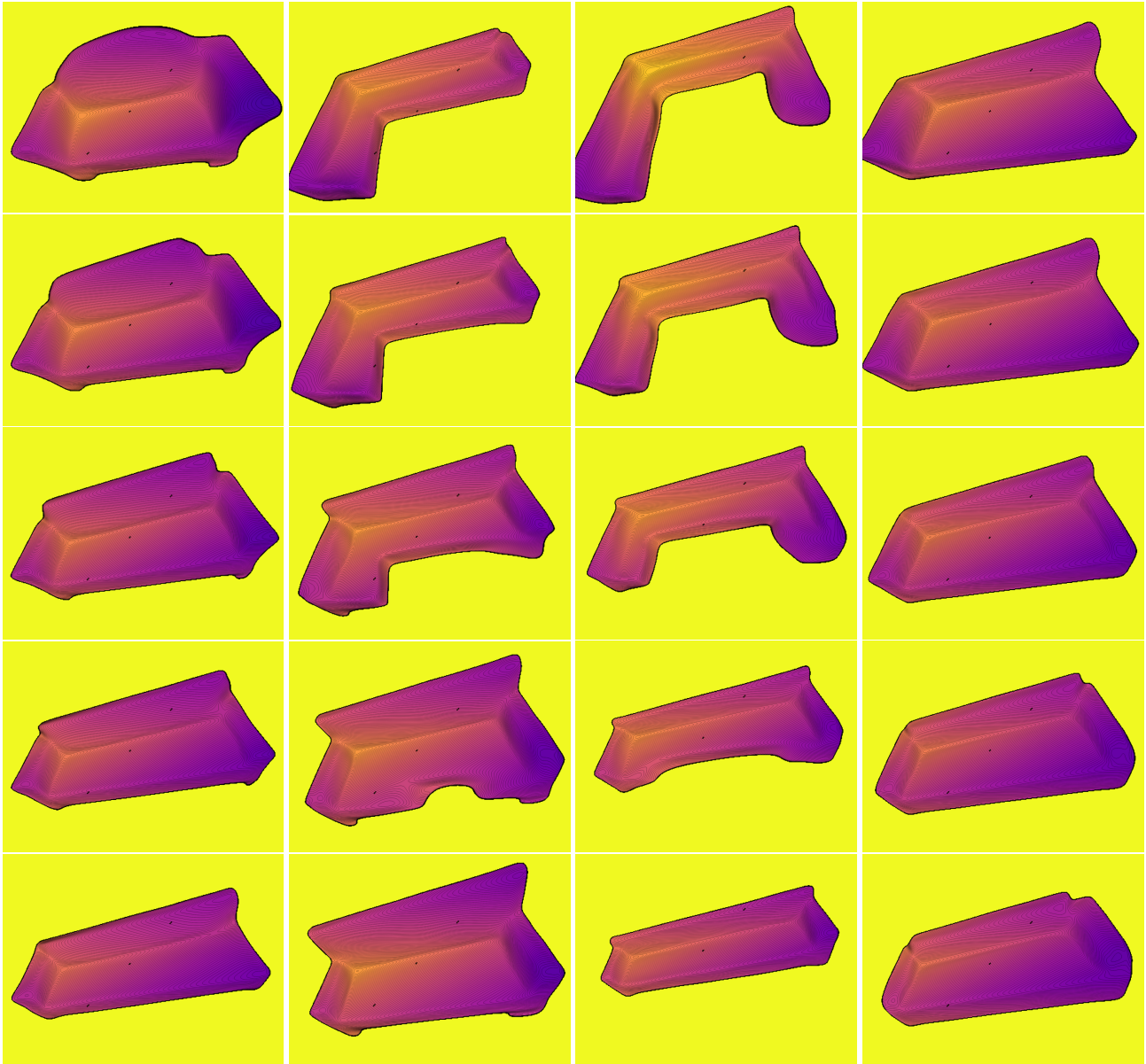


Figure 7. SDDF shape interpolation between two sofa instances. The first and last row show the SDDF output from the same view for two different instances from the training set. The rows in the middle are generated by using a weighted average of the latent codes of the upper-most and down-most instances as an input to the SDDF network. In each column, from top to bottom, the latent code weights with respect to the upper-most instance are 1, 0.75, 0.5, 0.25, 0, respectively. Note how the shapes transform smoothly from top to bottom with intermediate shapes looking like valid sofas. This demonstrates that the SDDF model represents the latent shape space continuously and meaningfully.

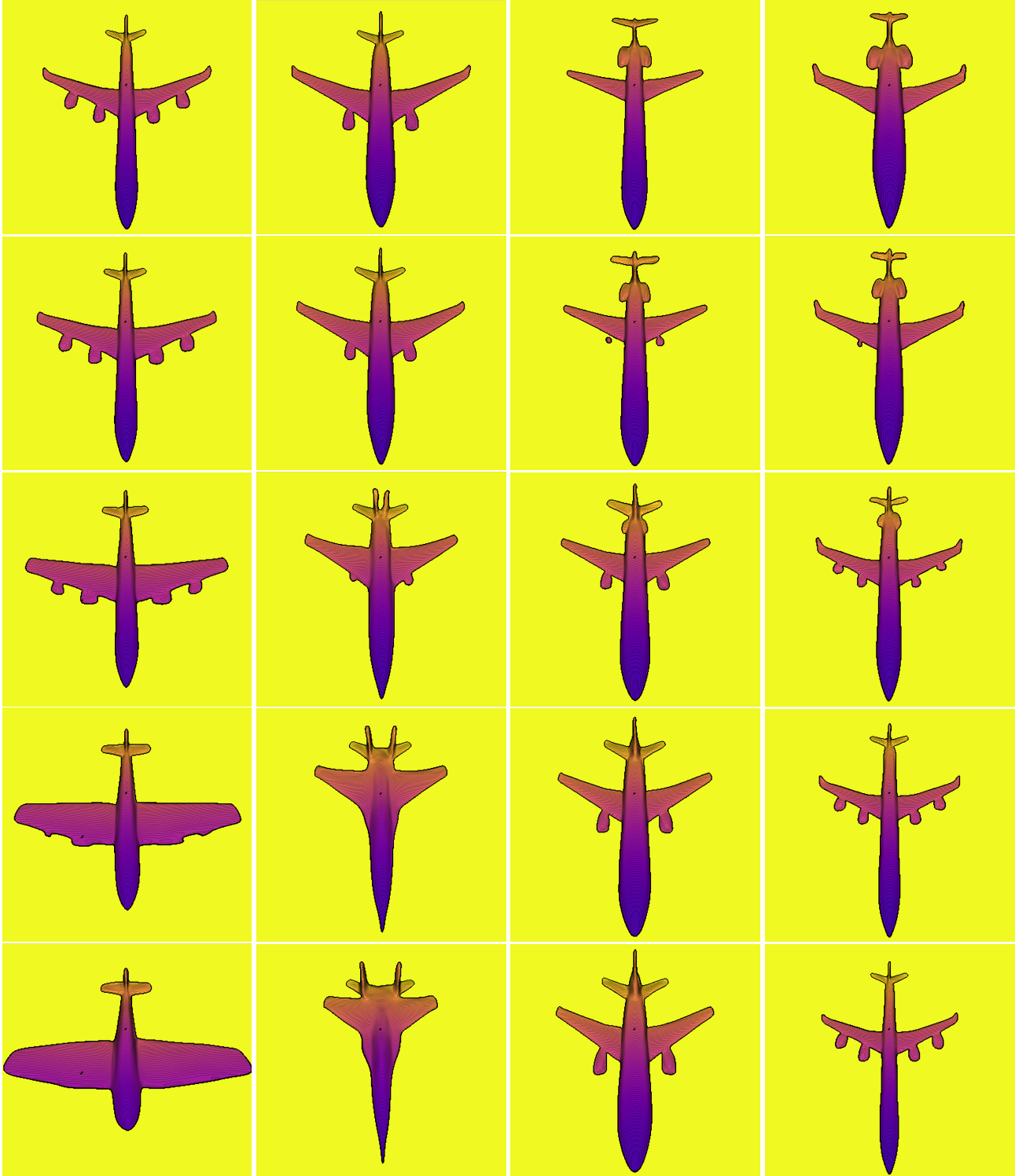


Figure 8. SDDF shape interpolation between two airplane instances. The first and last row show the SDDF output from the same view for two different instances from the training set. The rows in the middle are generated by using a weighted average of the latent codes of the upper-most and down-most instances as an input to the SDDF network. In each column, from top to bottom, the latent code weights with respect to the upper-most instance are 1, 0.75, 0.5, 0.25, 0, respectively. Note how the shapes transform smoothly from top to bottom with intermediate shapes looking like valid airplanes. This demonstrates that the SDDF model represents the latent shape space continuously and meaningfully.



Figure 9. SDDF shape interpolation between two car instances. The first and last row show the SDDF output from the same view for two different instances from the training set. The rows in the middle are generated by using a weighted average of the latent codes of the upper-most and down-most instances as an input to the SDDF network. In each column, from top to bottom, the latent code weights with respect to the upper-most instance are 1, 0.75, 0.5, 0.25, 0, respectively. Note how the shapes transform smoothly from top to bottom with intermediate shapes looking like valid cars. This demonstrates that the SDDF model represents the latent shape space continuously and meaningfully.

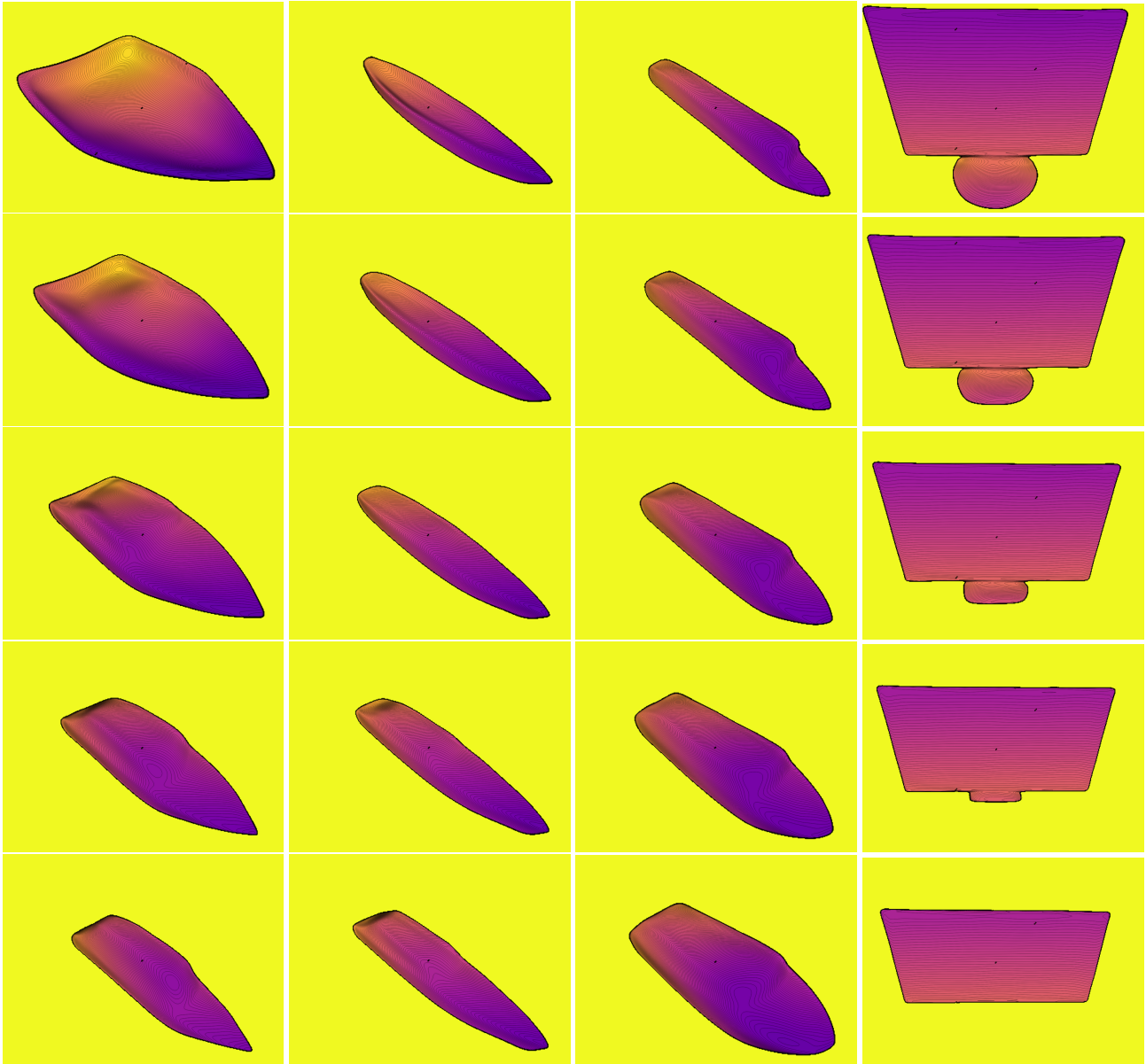


Figure 10. SDDF shape interpolation between two watercraft instances in the first three columns and two display instances in the last column. The first and last row show the SDDF output from the same view for two different instances from the training set. The rows in the middle are generated by using a weighted average of the latent codes of the upper-most and downer-most instances as an input to the SDDF network. In each column, from top to bottom, the latent code weights with respect to the upper-most instance are 1, 0.75, 0.5, 0.25, 0, respectively. Note how the shapes transform smoothly from top to bottom with intermediate shapes looking like valid instances. This demonstrates that the SDDF model represents the latent shape space continuously and meaningfully.

7.2. Effect of the Network Size on the Performance

This section evaluates the effect of the number of layers and number of neurons per layer in the SDDF model on the performance qualitatively and quantitatively. The results are obtained using a single sofa instance, shown in Fig. 3 in main paper. We use the same settings as the single-object experiment in Sec. 5.1 with data augmentation from 10k random views. The default model in the paper has 16 layers with 512 neurons per layer with skip connections every 4 layers.

First, we varied the number of layers in the neural network, while keeping a skip connection every 4 layers. We evaluated the SDDF model with 4 (with out skip connection), 8, 12, 16 layers. Quantitatively, as seen in Fig. 11, at first the error decreases significantly and then it increases slowly. Qualitatively, in Fig. 12, with more layers the model can capture finer details about the shape but even with 8 layers the shape is reconstructed very well.

Second, in the default setup with 16 layers, we kept an equal number of neurons per layer but varied the number as 8, 32, 128, 512. As we see in Fig. 11, at first the error decreases significantly and then continues to decrease slowly. In Fig. 13, we see that with fewer neurons per layer the model cannot capture the shape details very well. In comparison to the changing number of layers experiment, we see that the model is qualitatively more sensitive to the number of neurons.

7.3. Proof of Lemma 5

This section provides the proof of Lemma 5 and a brief intuitive discussion on difference of the spherical convex hull computation and its discretized approximation.

Lemma 5. *Let \mathcal{P} be a set of points on the unit sphere. The boundary points of \mathcal{P} with respect to \mathbf{e}_3 are points that are adjacent vertices to \mathbf{e}_3 in the convex hull of $\mathcal{P} \cup \{\mathbf{e}_3\}$. Let m be a function that maps a point on the unit sphere to the plane $z = 0$ with center \mathbf{e}_3 , i.e., $m([x, y, z]^\top) := [\frac{x}{1-z}, \frac{y}{1-z}]^\top$. A point $\mathbf{u} \in \mathcal{P}$ is a boundary point if and only if $m(\mathbf{u})$ is a vertex of the convex hull of $m(\mathcal{P})$.*

Proof. For $\mathbf{u} = [u_x, u_y, u_z]^\top \in \mathcal{P}$, suppose that $m(\mathbf{u})$ is not a vertex of the convex hull of $m(\mathcal{P})$. Then, there exists a set of points $\{\mathbf{u}^i = [u_x^i, u_y^i, u_z^i]^\top\}_{i=0}^n \subset \mathcal{P} \setminus \{\mathbf{u}\}$ and coefficients $\{\alpha_i\}_{i=0}^n$, $0 < \alpha_i < 1$, $\sum_{i=0}^n \alpha_i = 1$ such that $m(\mathbf{u}) = \sum_{i=0}^n \alpha_i m(\mathbf{u}^i)$. Let $\beta := \frac{1}{\sum_{i=0}^n \alpha_i \frac{1-u_z}{1-u_z^i}}$, and $\gamma_i = \beta \alpha_i \frac{1-u_z}{1-u_z^i}$, so that $\sum_{i=0}^n \gamma_i = 1$. Since all points are

on the unit sphere, we have $\gamma_i > 0$, $\beta > 0$, and:

$$\begin{aligned} \sum_{i=0}^n \gamma_i \mathbf{u}_x^i &= \beta(1-u_z) \sum_{i=0}^n \alpha_i \frac{u_x^i}{1-u_z^i} \\ &= \beta(1-u_z) \frac{u_x}{1-u_z} = \beta u_x, \\ \sum_{i=0}^n \gamma_i \mathbf{u}_z^i &= \beta(1-u_z) \sum_{i=0}^n (\alpha_i \frac{1-(1-u_z^i)}{1-u_z^i}) \\ &= \beta \sum_{i=0}^n \alpha_i \frac{1-u_z}{1-u_z^i} - \beta(1-u_z) (\sum_{i=0}^n \alpha_i) \\ &= 1 - \beta(1-u_z). \end{aligned}$$

Hence, $\sum_{i=0}^n \gamma_i \mathbf{u}^i = [\beta u_x, \beta u_y, 1 - \beta(1-u_z)]^\top = (1-\beta)\mathbf{e}_3 + \beta\mathbf{u}$. Note that $(1-\beta)\mathbf{e}_3 + \beta\mathbf{u}$ is on the segment from \mathbf{e}_3 to \mathbf{u} , so $0 < \beta < 1$; otherwise the convex combination of points on the unit sphere ($\sum_{i=0}^n \gamma_i \mathbf{u}^i$) will be out of unit sphere. This means that the segment between \mathbf{e}_3 and \mathbf{u} intersects with the convex hull of \mathcal{P} at another point $(1-\beta)\mathbf{e}_3 + \beta\mathbf{u}$, which implies that \mathbf{u} is not a boundary point of \mathcal{P} . The converse statement can be proven similarly by reversing the steps above. \square

For usual physically plausible objects, a few views (depending on the object shape complexity) with sufficiently high distance image resolution are sufficient to obtain a distance image from any other view using the convex hull approach described in Sec. 4.5 of the main paper. Intuitively, after transforming the object surface to a unit sphere with respect to an arbitrary point on the object surface, the region from which the sphere origin is observable may be decomposed into few convex regions. Hence, considering few distance views with sufficiently high resolutions should be sufficient to encode the real object shape. On the other hand, the discretized approximation of the convex hull is very efficient but its accuracy is limited by the azimuth resolution.

7.4. 2D Evaluation

This section shows that an SDDF model can be used in 2D, e.g., with distance measurements obtained from a LiDAR scanner. We simulated a Hokuyo UTM-30LX LiDAR scanner with 1081 rays per scan moving along a manually specified trajectory in an environment containing a 2D shape. See Fig. 14 for an example. The Lidar scans were used as training data for the SDDF and IGR models. After training, the SDDF network can generate distance values to the object contours at any location and in any viewing direction. Fig. 14 visualizes the models learned by IGR and SDDF for a heart-shaped 2D object. The distance predictions of the SDDF model are shown at every 2D location for several fixed viewing directions. We see that the SDDF model recognizes the boundary between free space and the object well. The parallel distance level sets indicate that

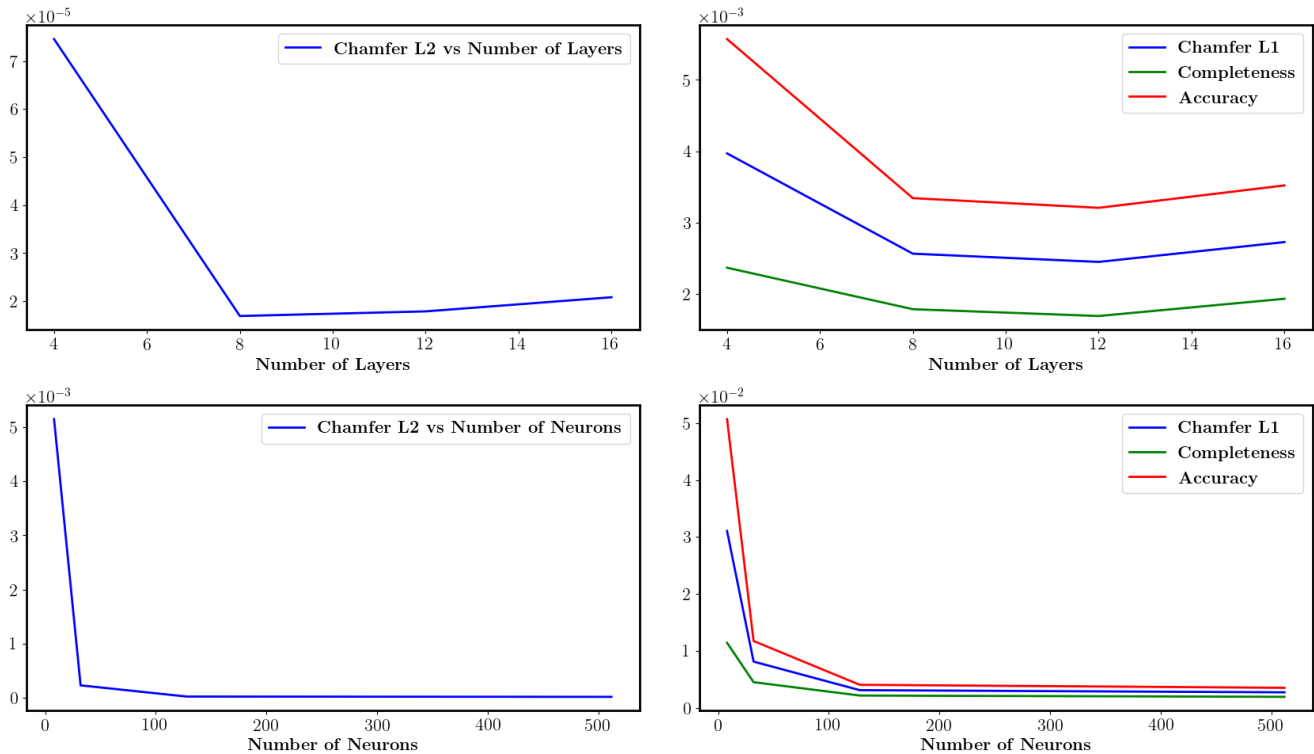


Figure 11. The first row shows the error as the number of layers changes between 4, 8, 12, 16 layers. The second row shows the error as number of neurons changes between 8, 32, 128, 512. In each row the left figure is Chamfer- L_2 distance, and the right one contains Chamfer- L_1 distance, Accuracy and Completeness.

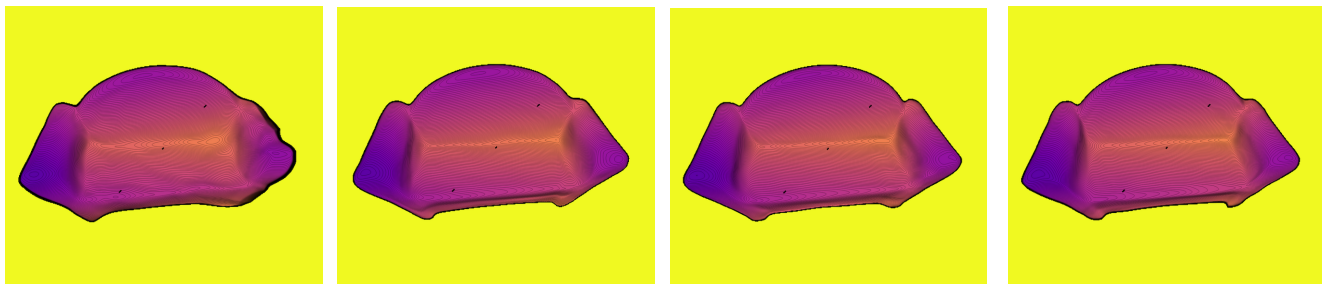


Figure 12. Distance views synthesized by our SDDF model trained with the same data with 512 neurons per layer and different numbers of layers: 4 (first), 8 (second), 12 (third), 16 (forth).

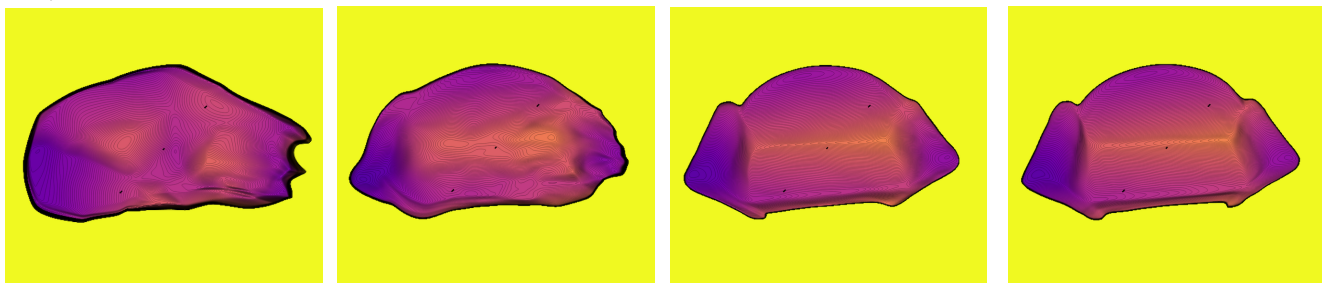


Figure 13. Distance views synthesized by our SDDF model trained with the same data with 16 layers and different numbers of neurons per layer: 8 (first), 32 (second), 128 (third), 512 (forth).

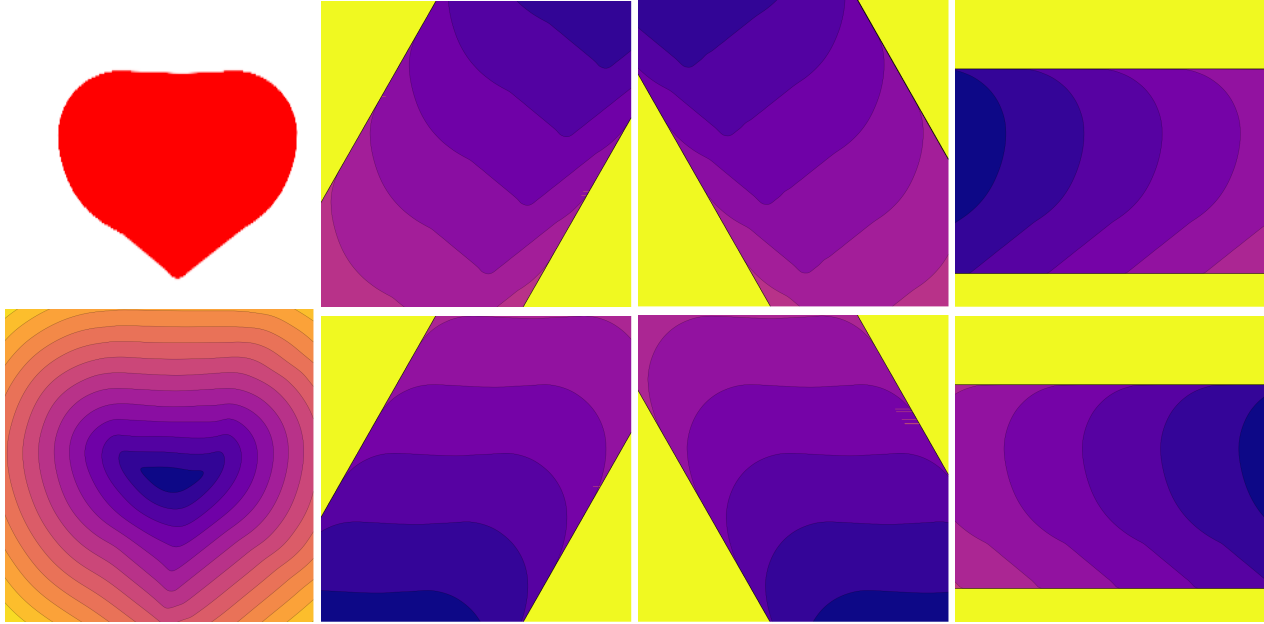


Figure 14. Ground-truth 2D instance (top left) and signed distance field (bottom left) learned by IGR [11]. The remaining plots show the output of our SDDF model with a fixed direction at each 2D location in the image. The fixed viewing directions for the six plots from left to right and top to down are $\frac{\pi}{3}$, $\frac{2\pi}{3}$, π , $\frac{4\pi}{3}$, $\frac{5\pi}{3}$, 2π , respectively. To produce good color contrast, in all images infinite distance values (corresponding to rays in free space) are set to 1.

the condition in Lemma 1 in the main paper indeed holds everywhere.

7.5. Small Training Set without Synthesized Data

In this section, we study the performance of the SDDF model when only a small training set is available and the data augmentation technique, described in Sec. 4.5 is not used. The results are generated using 100 car and 200 airplane instances from the ShapeNet dataset [4]. To generate training data, we use the functions in PyTorch3D [36] for ray casting. For each object, we choose 1000 random locations uniformly distributed on a sphere with orientations facing the object. Each distance image was down-sampled to have at most 5000 finite rays and 5000 infinite rays. An SDDF model with 8 fully connected layers, 512 hidden units per layer, and a skip connection from the input to the middle layer is used. All experiments are done on a single GTX 1080 Ti GPU using PyTorch [34] and the ADAM optimizer [18] with initial learning rate of 0.005.

Single Instance Shape Representation. For single-instance shape estimation, we schedule the learning rate to decrease by a factor of 2 every 500 steps for $9k$ iterations. In each iteration, we pick a batch of 128^2 samples randomly from the input data. The result is provided in Fig. 15.

Shape Completion and Interpolation. For Car category-level shape estimation, the network is trained for 500 epochs with 100 instances. The learning rate is scheduled to decrease by a factor of 2 every 50 epochs. In each iteration, for each shape, 8000 random samples are picked uniformly out of the training data for that instance. For the Airplane category, the network is trained for 5000 epochs with 200 shapes. The learning rate is scheduled to decrease by a factor of 2 every 250 epochs. In each iteration, for each instance $10k$ random samples are picked uniformly. Shape completion results are provided in Fig. 16, while shape interpolation results are provided in Fig. 17.

Effect of Measurement Noise on the Performance. We present qualitative and quantitative results about the effects of noisy distance data and different number of layers and neurons per layer in the model on the performance of the SDDF model. The results are obtained for a single Airplane instance, shown in Fig. 15. We obtained 500 finite rays and 500 infinite rays from 1000 random locations uniformly distributed on a sphere around the instance with orientations facing the object. The SDDF model was trained for $9k$ iterations in several different settings. The default setting has 8 layers with 512 neurons per layer and noise-free distance data for training. Training this model takes about 688 seconds. A distance view synthesized by the trained SDDF model is shown in Fig. 18.

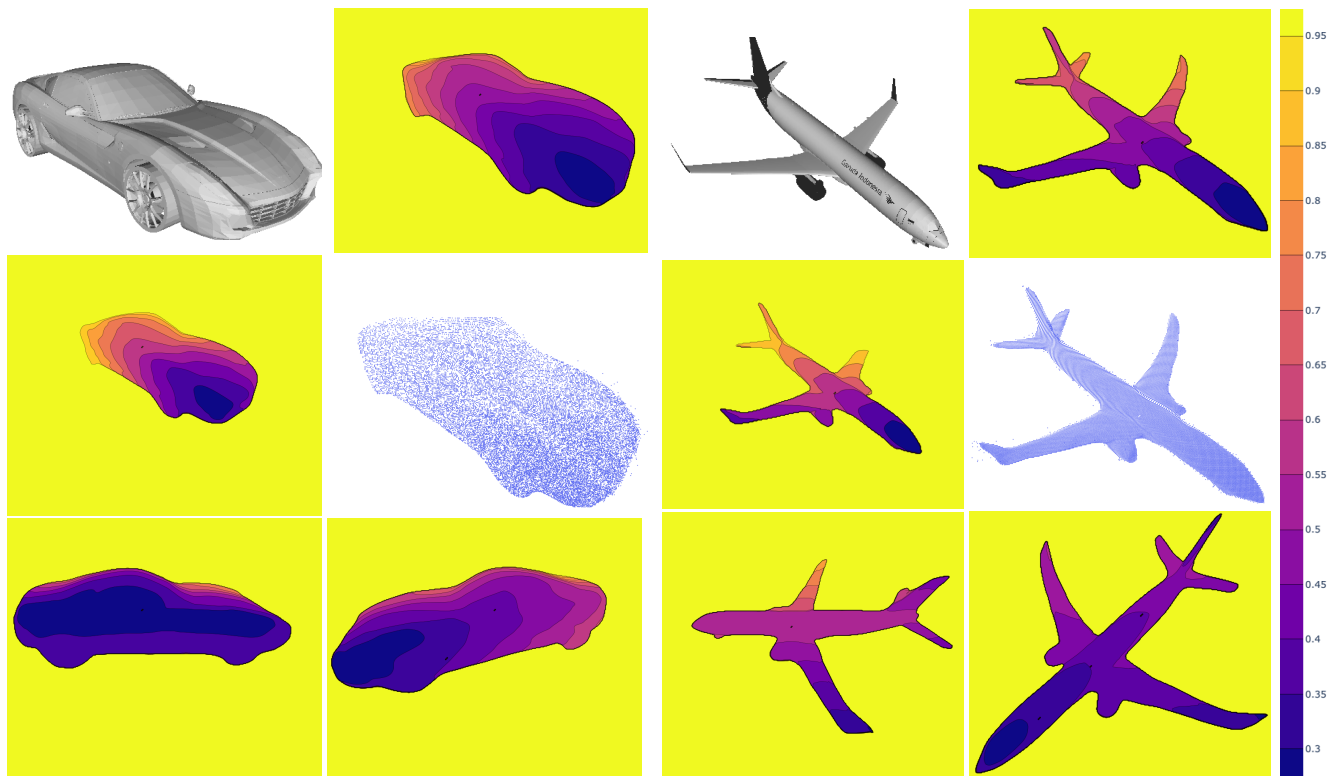


Figure 15. SDDF shape representation of a car (left two columns) and airplane (right two columns) instance. In each two columns, the ground-truth model is shown on the top left, a distance image synthesized by the SDDF model is shown on the top right, and a point cloud generated from the distance image is shown in the middle right. The middle left shows a distance image synthesized from the same view but further distance from the object. Note that the level sets in the distant view remain parallel to the close-up view but more yellowish, indicating the distance increase. The third row includes more distance images synthesized by our SDDF model from other views. To produce good color contrast, in all images we set infinite distance values (corresponding to rays in free space) to 1.

First, keeping the network structure fixed, we varied the standard deviation of zero-mean Gaussian noise added to the distance measurements. To have a sense about the noise magnitude, note that the radius of the sphere on which the camera locations were picked was 0.6. Qualitatively, as we see in Fig. 19, the more the noise increases, the fewer details the SDDF model can capture. Second, we varied the number of layers (fixing the number of neurons to 512) and the number of neurons (fixing the number of layers to 8) in the neural network, keeping a skip connection to the middle layer, to measure the training, as shown in Fig. 18.

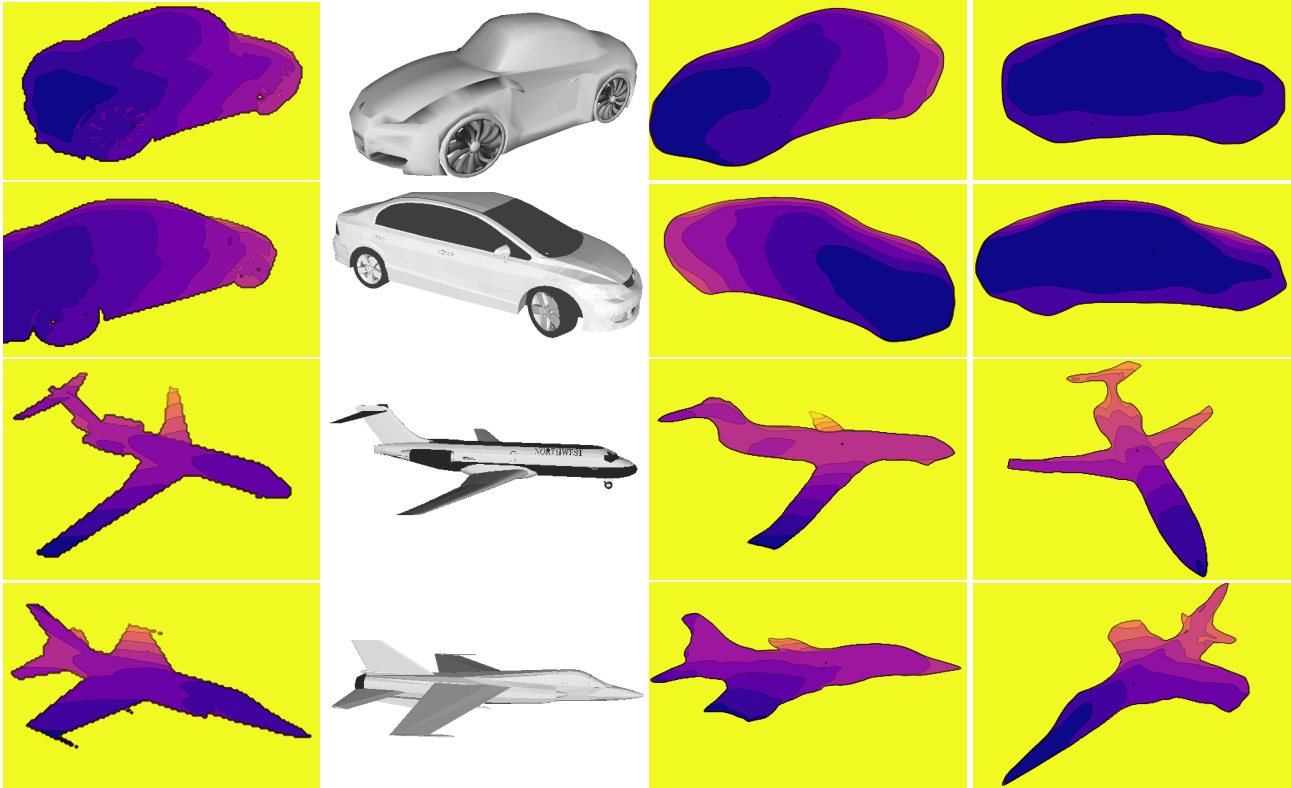


Figure 16. SDDF shape completion using a distance image (left column) from an unseen object instance (second column). After latent code optimization, the SDDF model can synthesize novel distance views (third and fourth columns).

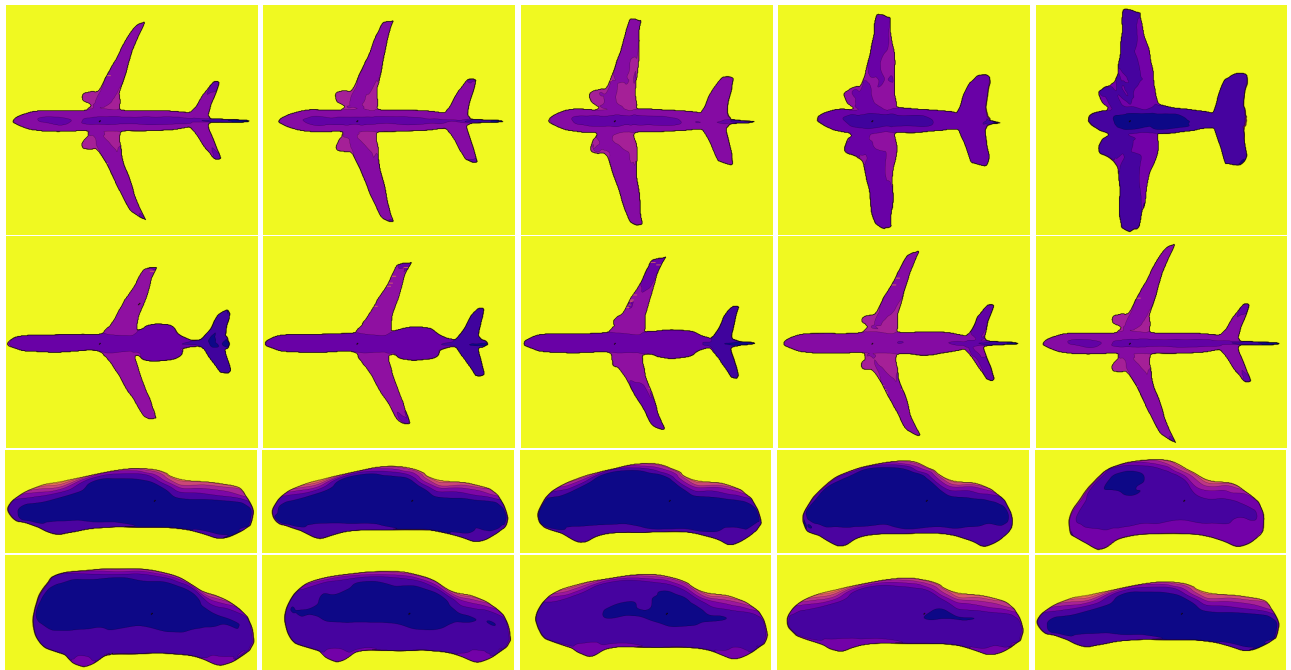


Figure 17. SDDF shape interpolation between two instances. The left-most and right-most columns show the SDDF output from the same view for two different instances from the training set. The three columns in the middle are generated by using a weighted average of the latent codes of the left-most and right-most instances as an input to the SDDF network. In each row, from left to right, the latent code weights with respect to the left-most instance are 1, 0.75, 0.5, 0.25, 0, respectively. Note how the shapes transform smoothly from the left-most to the right-most instances with intermediate shapes looking like valid cars and airplanes. This demonstrates that the SDDF model represents the latent shape space continuously and meaningfully.

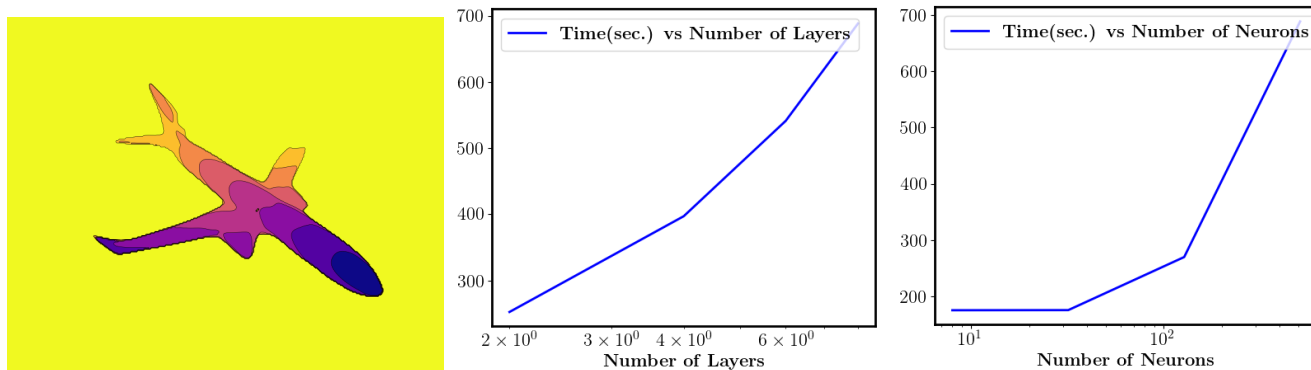


Figure 18. Distance image (left) produced by our SDDF model with 8 layers, 512 neurons per layer, and noiseless training data. The model training time is shown as a function of the number of layers (middle) and number of neurons per layer (right). Note that in the right plot the x -axis is in log scale and the number of neurons is equal in all layers. The error of the point cloud, obtained from 100 distance images produced by our SDDF model at 100 fixed poses, with respect to the ground-truth instance mesh in different settings: noisy distance data (left), changing number of network layers (middle), and changing numbers of neurons per layer (right). Note that in the right plot the x -axis is in log scale and the number of neurons is equal in all layers.

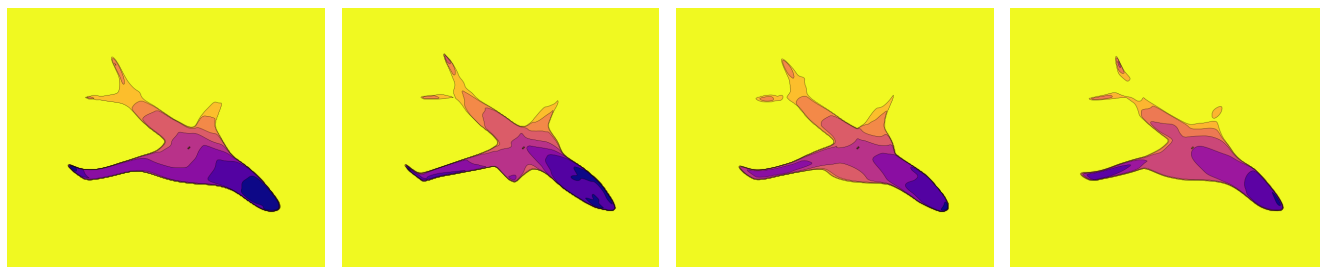


Figure 19. Distance views synthesized by our SDDF model with default structure (8 layers and 512 neurons per layer) trained on noisy data. The standard deviation of the Gaussian noise added to the distance data from left to right is 0.1, 0.2, 0.3, 0.4, respectively.